DOI: 10.1002/chem.200801615

Intervalent Bis(μ-aziridinato)M^{II}–M^{I} Complexes (M = Rh, Ir): Delocalized Metallo-Radicals or Delocalized Aminyl Radicals?

Cristina Tejel,*[a] Miguel A. Ciriano,[a] Vincenzo Passarelli,[a] José A. López,[a] and Bas de Bruin*[b]

Dedicated to Professor Ernesto Carmona on the occasion of his 60th birthday

Abstract: Reactions of the methoxo complexes [{M(μ-OMe)(cod)}$_2$] (cod = 1,5-cyclooctadiene, M = Rh, Ir) with 2,2-dimethylaziridine (Haz) give the mixed-bridged complexes [{M_2(μ-az)(μ-OMe)(cod)$_2$}] [(M = Rh, **1**; M = Ir, **2**). These compounds are isolated intermediates in the stereospecific synthesis of the amido-bridged complexes [{M(μ-az)(cod)}$_2$] (M = Rh, **3**; M = Ir, **4**). The electrochemical behavior of **3** and **4** in CH_2Cl_2 and CH_3CN is greatly influenced by the solvent. On a preparative scale, the chemical oxidation of **3** and **4** with [$FeCp_2$]$^+$ gives the paramagnetic cationic species [{M(μ-az)(cod)}$_2$]$^+$ (M = Rh, [**3**]$^+$; M = Ir, [**4**]$^+$). The Rh complex [**3**]$^+$ is stable in dichloromethane, whereas the Ir complex [**4**]$^+$ transforms slowly, but quantitatively, into a 1:1 mixture of the allyl compound [(η^3,η^2-C_8H_{11})Ir(μ-az)$_2$Ir(cod)] ([**5**]$^+$) and the hydride compound [(cod)(H)Ir(μ-az)$_2$Ir(cod)] ([**6**]$^+$). Addition of small amounts of acetonitrile to dichloromethane solutions of [**3**]$^+$ and [**4**]$^+$ triggers a fast disproportionation reaction in both cases to produce equimolecular amounts of the starting materials **3** and **4** and metal–metal bonded M^{II}–M^{II} species. These new compounds are isolated by oxidation of **3** and **4** with [$FeCp_2$]$^+$ in acetonitrile as the mixed-ligand complexes [$(MeCN)_3$M(μ-az)$_2$M(NCMe)(cod)](PF_6)$_2$ (M = Rh, [**8**]$^{2+}$; M = Ir, [**9**]$^{2+}$). The electronic structures of [**3**]$^+$ and [**4**]$^+$ have been elucidated through EPR measurements and DFT calculations showing that their unpaired electron is primarily delocalized over the two metal centers, with minor spin densities at the two bridging amido nitrogen groups. The HOMO of **3** and **4** and the SOMO of [**3**]$^+$ and [**4**]$^+$ are essentially M–M d–d σ*-antibonding orbitals, explaining the formation of a net bonding interaction between the metals upon oxidation of **3** and **4**. Mechanisms for the observed allylic H-atom abstraction reactions from the paramagnetic (radical) complexes are proposed.

Keywords: aminyl radicals · C–H activation · iridium · metalloradicals · rhodium

Introduction

The reduction or oxidation of closed-shell metal complexes often provides interesting and unexpected electronic distributions and reaction pathways.[1] The nature of the metal center and the ligands plays a crucial role in determining the outcome of the electron-transfer reaction resulting in metal-centered and ligand-centered processes, which are well documented in the literature for group 9 transition metals.[2] When applied to the electron rich amido/alkoxo complexes of these metals, the one-electron oxidation could result in a redox isomerism between the amido/alkoxo and the aminyl/alkoxyl forms (Scheme 1). Grützmacher et al. have recently reported that the one-electron oxidation of mononuclear amido rhodium(I) complexes based on the dibenzo[*a,d*]cycloheptene-5-yl platform produces unprecedented, thermally stable, aminyl radical complexes, species

---

[a] Dr. C. Tejel, Prof. Dr. M. A. Ciriano, Dr. V. Passarelli,
Dr. J. A. López
Instituto de Ciencia de Materiales de Aragón (ICMA)
CSIC-UZ, Pedro Cerbuna 12, E-50009 Zaragoza (Spain)
Fax: (+34) 976-791187
E-mail: ctejel@unizar.es

[b] Dr. B. de Bruin
Van't Hoff Institute for Molecular Sciences
University of Amsterdam
Nieuwe Achtergracht 166, 1018 WV Amsterdam (The Netherlands)
Fax: (+20) 525-5604
E-mail: b.debruin@uva.nl

Supporting Information for this article is available on the WWW under http://dx.doi.org/10.1002/chem.200801615.

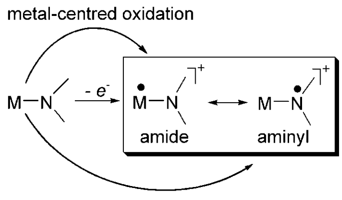

Scheme 1. Resonance forms of radical amide/aminyl complexes.

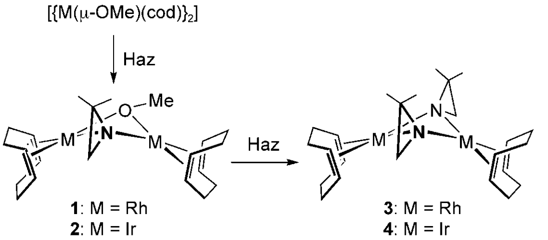

Scheme 2. Synthesis of complexes **1**–**4** (Haz = 2,2-dimethylaziridine).

in which the unpaired electron mainly resides on the nitrogen atom.[3] Moreover, the related iridium aminyl radicals are efficient catalysts in the dehydrogenation of functionalized primary alcohols to the corresponding aldehydes.[4]

A survey of the literature on this topic made us aware of the absence of data about the redox behavior of dinuclear Rh^{I} and Ir^{I} amido derivatives. Dinuclear amido complexes of these metals are well-known,[5] and some of them have been reported as useful precursors for the synthesis of imido complexes,[6] for the transfer of the amido group to olefins,[7] and in catalyzed C–C bond formation reactions.[8] Further, studies of the oxidative addition reactions of halocarbons allowed the synthesis of Ir^{I}/Ir^{III} derivatives[9] and the detection of S_N^2 profiles in the activation of chloro compounds.[10]

Herein we report on the synthesis of new dinuclear amido complexes of rhodium and iridium derived from aziridines as well as on their electrochemical behavior. We were searching for dinuclear complexes with aminyl radical character. The choice of the aziridine molecule as ligand was not arbitrary. Aziridines are extremely useful and versatile functional reagents in organic synthesis,[11] with an inherent reactivity toward ring opening with a wide range of nucleophiles.[12] However, there are only two reports on the reactions of aziridines with late transition metal complexes that afford isolable aza-metalla-cyclobutanes,[13] despite the fact that they have been invoked as intermediates in catalytic transformations. This possibility has not been reported for rhodium and iridium yet, for which the coordination and organometallic chemistry with aziridines is still poorly developed.[14]

Results and Discussion

Synthesis and characterization of complexes 1–4: The reaction of the methoxo derivatives [{M(μ-OMe)(cod)}$_2$] (cod = 1,5-cyclooctadiene, M = Rh, Ir) with 2,2-dimethylaziridine (Haz) in toluene produces the mixed bridging-ligand complexes [{M(cod)}$_2$(μ-az)(μ-OMe)] (M = Rh (**1**), Ir (**2**), Scheme 2), which did not spontaneously proceed to exchange the aziridine for the methoxo fragment, even in the presence of an excess of the aziridine. Because the incorporation of the aziridinato ligand into the dinuclear entity is associated with the elimination of methanol, the synthesis of the bis(μ-aziridinato) complexes [{M(μ-az)(cod)}$_2$] (M = Rh (**3**), Ir (**4**), Scheme 2) was achieved by refluxing [{M(μ-OMe)(cod)}$_2$] and 2,2-dimethylaziridine in toluene in the presence of molecular sieves (5 Å). This methodology represents an easy and clean way to deprotonate poorly acidic ligands, because the elimination of methanol from the reaction media shifts the reaction to completion. Once isolated, complexes **1**–**4** are stable in the air for months.

A view of the molecular structure of **2** is shown in Figure 1. Selected bond lengths and angles are given in Table 1. The oxygen and the nitrogen atoms from the bridging methoxo and aziridinato ligands, respectively, together with a 1,5-cyclooctadiene ligand on each metal, complete a distorted square-planar coordination geometry for both metal atoms. The centroids of the olefinic bonds (Ct1-Ct4) are located 0.136(7), 0.091(7), 0.204(6) and 0.106(7) Å, respectively, below the IrN$_2$ planes, directed towards the pocket of the complex. The four-membered ring "IrNIrO" shows a folded conformation (dihedral angle between the coordination planes defined by O1-Ir1-N2 and O1-Ir2-N2 is

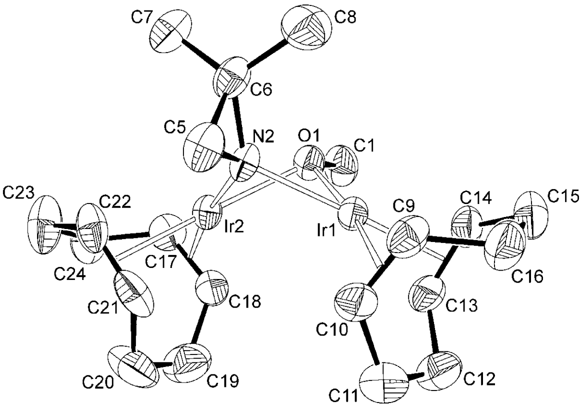

Figure 1. Structure (ortep at 50 % level) of complex **2**.

Table 1. Selected bond lengths [Å] and angles [°] for complex **2**.

Ir1–O1	2.083(4)	Ir2–O1	2.089(4)
Ir1–N2	2.068(4)	Ir2–N2	2.068(4)
Ir1–Ct1	1.966(7)	Ir2–Ct3	1.999(6)
Ir1–Ct2	1.990(7)	Ir2–Ct4	1.952(7)
O1-Ir1-N2	74.22(16)	O1-Ir2-N2	74.35(16)
O1-Ir1-Ct1[a]	171.3(2)	O1-Ir2-Ct3[a]	99.7(2)
O1-Ir1-Ct2[a]	171.3(2)	O1-Ir2-Ct4[a]	171.5(2)
Ir1-O1-Ir2	85.01(14)	Ir1-N2-Ir2	85.62(16)

[a] Ct1, Ct2, Ct3 and Ct4 are the midpoints between C9-C10, C13-C14, C17-C18 and C21-C22, respectively.

116.44(12)°), which produces a relatively short intermetallic distance (2.8191(4) Å).

Regarding the groups connected to the bridging atoms, the relative positions of the methyl fragment on the oxygen (equatorial) and the $C(Me)_2$ fragment (axial) define a bent-*anti-a* stereochemistry[5e] and, on the whole, the structure of **2** was found to be similar to previously reported amido/alkoxo or amido/methoxo complexes of late transition metals.[5e]

The molecular structure of complex **3** is shown in Figure 2 and Table 2 collects the selected bond lengths and angles. In complex **3**, two rhodium centers are bridged by the nitrogen atoms of two aziridinato ligands, and a distorted square-planar coordination geometry for each metal is completed by the 1,5-cyclooctadiene groups. Again, the centroids of the olefinic bonds (Ct1 and Ct2) are shifted from the RhN2 plane towards the pocket of the complex by 0.080(4) and 0.403(4) Å, respectively. Notably, a rather short intermetallic distance in **3**, 2.7868(5) Å is observed. Accordingly, the angle between the coordination planes defined by N1-Rh1-N2 and N1-Rh2-N2 is quite small 117.78(8)°. Related dinuclear rhodium(I) amido complexes showed longer intermetallic distances, which are associated with wider folding angles of the four-membered metallacycles.[5d]

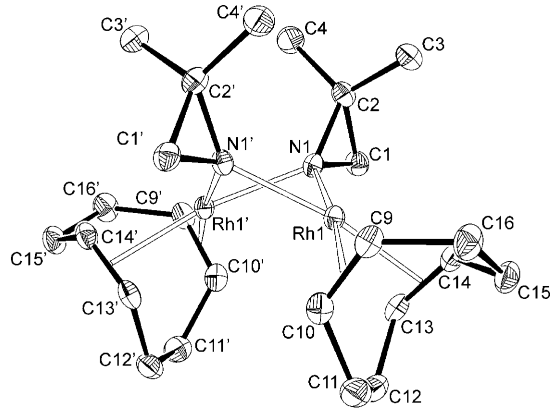

Figure 2. Structure (ortep at 50% level) of complex **3**.

Table 2. Selected bond lengths [Å] and angles [°] for complex **3**[a].

Rh1−N1	2.078(3)	Rh1−Ct1	2.004(4)
Rh1−N1′	2.091(3)	Rh1−Ct2	1.997(4)
N1-Rh1-N1′	77.34(13)	N1-Rh1-Ct1[b]	174.08(13)
Rh1-N1-Rh1′	83.89(11)	N1-Rh1-Ct2[b]	96.91(13)

[a] Primed atoms are related to the unprimed ones by the symmetry operation $-x+\frac{1}{2}$, $-y+\frac{1}{2}$, z. [b] Ct1 and Ct2 represent the centroids of the olefinic bonds C9−C10 and C13−C14, respectively.

We ascribe the relatively short metal–metal distances and the folded geometries of **3** and **4** to special binding interactions of the aziridinato ligands revealed by DFT calculations. Although a straightforward interpretation of the bonding orbital interactions in the optimized geometries (b3-lyp, TZVP) of **3** and **4** is somewhat complicated by these bonding interactions being spread-out over several molecular orbitals, it is clear that they are dominated by 3c-4e interactions between the two metal atoms and the aziridinato nitrogen atoms (Figure 3).

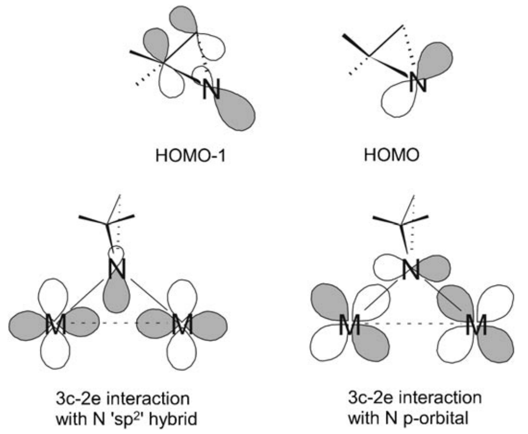

Figure 3. Simplified representation of the 3c-4e bonding interactions between the aziridinato fragments (top) and the metal centers in **3** and **4** as derived from DFT calculations (b3-lyp, TZVP).

The nitrogen p-orbital is the sole contributing atomic orbital to the HOMO of the aziridinate anion, whereas the HOMO-1 is essentially a nitrogen sp^2 hybrid orbital in bonding combination with two p-orbitals at the adjacent carbon units (a so-called banana bond). Both the aziridinate anion HOMO and HOMO-1 are involved in 3c-4e interactions with the two metal atoms in **3** and **4** as depicted in Figure 3 (see the Supporting information for some representative orbitals). The 3c-2e interaction with the nitrogen "sp^2 hybrid" results in a net metal–metal interaction, thus explaining the relatively short metal–metal distances (see Table 2 for the experimental distances and Table 5 for the calculated distances).

In solution NMR spectra, the mixed-ligand complexes **1** and **2** reveal only one isomer, showing the symmetry plane bisecting the N and O atoms. This one species observed in solution should correspond to the stereoisomer found in the solid-state (*bent-anti-a*),[5e] as deduced from the nOe enhancements observed for the two closest olefinic protons upon irradiation of the CH_2 protons from the aziridine group and the methyl group from the methoxo ligand.

NMR spectra of complexes **3** and **4** also indicated the presence of only one isomer in solution. Analysis of their NMR data indicated that they possess *syn* configurations (as found in the solid state for **3**) (Figure 4), as deduced from the C_{2v} symmetry reflected by the spectra. Thus, six cod signals and two singlets for the equivalent methyl and methylene protons of the aziridinato fragment, respectively, were observed in the ^1H NMR spectra. Furthermore, the NOESY spectra revealed the expected nOe cross-peaks between the methyl protons of the aziridinato ligand and the olefinic protons outside of the pocket of the complexes. In addition, the methylenic protons of the aziridinato ligand produced

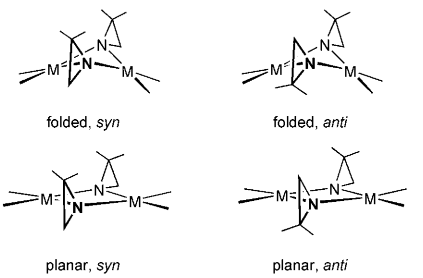

Figure 4. Configurations and conformations for bis(μ-aziridinato) complexes.

nOe cross-peaks with the olefinic protons inside and outside of the pocket, suggesting that the complexes are static on the NMR time scale, and do not display inversion of the four-membered M_2N_2 metallacycle as is usually observed in related dinuclear complexes.[15]

The stereospecific formation of **3** and **4** as the folded *syn* configurations only is noteworthy. The geometries remain unmodified even after prolonged heating under reflux in toluene. This was quite surprising to us, because the related bis(μ-amido) compounds derived from anilines [{M(μ-NHR)(cod)}$_2$] (R=Ph, 4-MeC$_6$H$_4$), isolated as the *syn* configurations (the kinetic product), readily equilibrate to *syn*/*anti* mixtures at room temperature in solution.[5d] We argue, for the aniline complexes, that the bulkiness of ancillary and bridging ligands is the driving force for the isomerization to the *anti* isomers (the thermodynamic products) and, in fact, the related compound [{Rh(μ-NH*t*Bu)(cod)}$_2$], with the even bulkier *tert*-butyl group was directly isolated having an *anti* configuration. We thus wondered whereas the folded *syn* configurations of **3** and **4** are also the kinetic products, or in this case also the thermodynamically preferred products. Therefore we decided to investigate this further with DFT.

The planar (*syn* and *anti*) conformations are not stable according to DFT calculations (b3-lyp, TZVP), and geometry optimizations in all cases converged to the folded geometries. The folded *syn* isomers of **3** and **4** are most stable. The folded *anti* isomers of **3** and **4** are +5.6 kcal mol^{-1} and +5.9 kcal mol^{-1} higher in energy than the folded *syn* isomers, respectively. Thus, isomerization of the folded *syn* isomers to the folded *anti* isomers is not to be expected for thermodynamic reasons, in good agreement with the experimental findings.

Redox behavior of complexes 3 and 4: The electrochemistry of complexes **3** and **4** was investigated by linear-sweep voltammetry (rotating-disk electrode; RDE) and cyclic voltammetry. The oxidation response of the dinuclear complex **3** at the RDE at room temperature in dichloromethane over the potential range 1500 to −1500 mV (vs SCE) consists of two well-defined oxidation waves with similar limiting currents per concentration unit. The reversibility of these oxidations was established by cyclic voltammetry, as well-shaped reduction waves were seen in the backward scan (Figure 5, top).

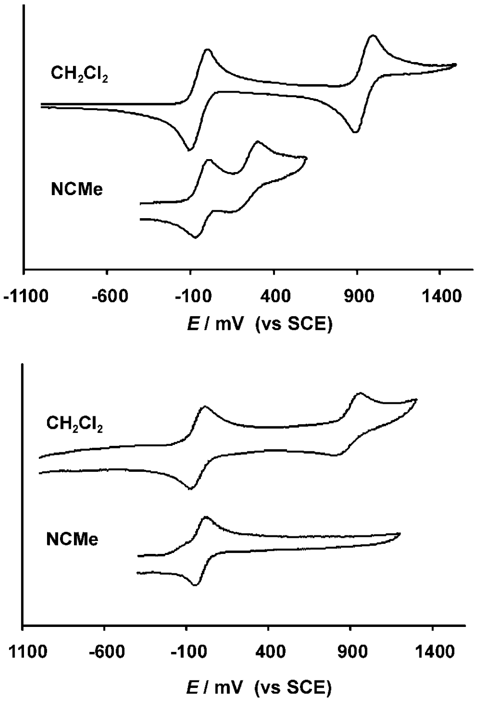

Figure 5. Cyclic voltammograms for complexes **3** (top) and **4** (bottom) in dichloromethane and acetonitrile. *E* values are given in mV versus SCE.

The characteristics of these waves are $E_1^0=-40$, $E_2^0=967$ mV; $\Delta E_p=75$, 76 mV, $I_b/I_f=1.01$, 0.99 and i_{Pa} versus $v^{1/2}$ constant. Thus, compound **3** is electrochemically oxidized by two stepwise, reversible one-electron transfers, showing an EE oxidation mechanism (EE: electron transfer, electron transfer), which can be reasonably attributed to the [**3**]/[**3**]$^+$ and [**3**]$^+$/[**3**]$^{2+}$ couples.

Analogous oxidation processes were observed in dichloromethane solutions for the iridium counterpart, complex **4** (Figure 5, bottom). The couple **4**/[**4**]$^+$ appears as a reversible one-electron redox process ($E^0=-28$ mV; $\Delta E_p=76$ mV, $I_b/I_f=1.00$, and i_{Pa} versus $v^{1/2}$ constant), whereas the couple **4**$^+$/[**4**]$^{2+}$ ($E_{Pa}=896$ mV) was found to be quasi-reversible, indicating that structural changes or further reactions are taking place on the time scale of the experiment. On the whole, the CV measurements reveal subsequent EEC$_{irr}$ (EEC$_{irr}$: electron transfer, electron transfer and irreversible chemical reaction) processes for the oxidation of iridium complex **4**.

The two oxidation waves are well separated by 1007 mV (**3**) and 924 mV (**4**), indicative of a reasonable stability for the radicals [**3**]$^+$ and [**4**]$^+$ towards a disproportionation reaction into the neutral (**3**, **4**) and dicationic ([**3**]$^{2+}$, [**4**]$^{2+}$) complexes, respectively. The estimated K_{disp} values were found to be 3.2×10^{-18} ($\Delta G^0=23.2$ kcal mol^{-1}) for the rhodium complex ([**3**]$^+$) and 8.9×10^{-17} ($\Delta G^0=21.3$ kcal mol^{-1}) for the iridium counterpart ([**4**]$^+$).

In a coordinating solvent like acetonitrile (Figure 5) a considerable shift of the second wave to lower potentials is observed in both cases. The effect is most substantial for the iridium complex, for which both oxidation processes collapse to a single wave (at 21 mV) in MeCN, as a consequence of the E_2^0 potential being $\leq E_1^0$. This clearly indicates $\mathbf{4}^+$ to be thermodynamically unstable in acetonitrile with respect to disproportionation into **4** and $\mathbf{4}^{2+}$. Thus, the wave in Figure 5 (bottom) should correspond to a two-electron oxidation process. For the rhodium counterpart, $\mathbf{3}^+$, the K_{disp} value in acetonitrile can be estimated at $\approx 5.3\times10^{-5}$ from the 250 mV separation between the two detectable waves (−30 and 220 mV). Although the first couple **3**/$\mathbf{3}^+$ corresponds to an E mechanism, the oxidation of $\mathbf{3}^+$ into $\mathbf{3}^{2+}$ is followed by a chemical reaction, probably with the solvent, according to the shape of the reduction wave in the reverse scan.

The strong influence of the solvent on the redox potentials of the complexes **3** and **4** is noteworthy. From the two well-separated waves observed in dichloromethane, two close waves for **3**, collapsing to a single one for **4**, are detected in the coordinating solvent acetonitrile. We wondered whether this is an effect of solvent destabilization of the mono-cationic species $[\mathbf{3}]^+$ and $[\mathbf{4}]^+$ or solvent stabilization of the final dicationic species $[\mathbf{3}]^{2+}$ and $[\mathbf{4}]^{2+}$. To shed some light on this observation we decided to optimize the mono and bis-acetonitrile adducts with DFT (b3-lyp, TZVP). Neither the neutral species (**3** and **4**) nor the mono-cationic species ($[\mathbf{3}]^+$ and $[\mathbf{4}]^+$) form stable MeCN adducts according to these calculations. Attempts to optimize the geometries of mono- and bis-MeCN adducts in all these cases led to spontaneous MeCN dissociation from the metal, and the geometries finally converged to unmodified species **3**, **4**, $[\mathbf{3}]^+$, and $[\mathbf{4}]^+$. Apparently, MeCN activation does not explain the easier oxidation of $[\mathbf{3}]^+$ and $[\mathbf{4}]^+$ in MeCN. The dicationic species $[\mathbf{3}]^{2+}$ and $[\mathbf{4}]^{2+}$, on the other hand, are substantially stabilized by MeCN coordination (Scheme 3). According to the DFT calculations, the mono-MeCN adducts $[\mathbf{3}(\mathrm{NCMe})]^{2+}$ and $[\mathbf{4}(\mathrm{NCMe})]^{2+}$ are about 20 kcal mol^{-1}, and the bis-MeCN adducts $[\mathbf{3}(\mathrm{NCMe})_2]^{2+}$ and $[\mathbf{4}(\mathrm{NCMe})_2]^{2+}$ about 30 kcal mol^{-1}, more stable than the bare dicationic species $[\mathbf{3}]^{2+}$ and $[\mathbf{4}]^{2+}$. These energy values are not corrected for entropy effects, but these do not likely play a large role in the experimental system anyway, where MeCN is used as the solvent.

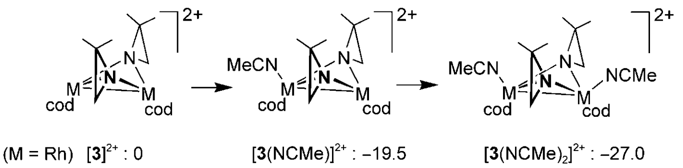

Scheme 3. Relative energies (kcal mol^{-1}) of DFT (b3-lyp, TZVP) optimized geometries $[\mathbf{3}]^{2+}$, $[\mathbf{4}]^{2+}$, $[\mathbf{3}(\mathrm{NCMe})]^{2+}$, $[\mathbf{4}(\mathrm{NCMe})]^{2+}$, $[\mathbf{3}(\mathrm{NCMe})_2]^{2+}$ and $[\mathbf{4}(\mathrm{NCMe})_2]^{2+}$.

The DFT calculations thus suggest that the marked easier electrochemical oxidation of $[\mathbf{3}]^+$ and $[\mathbf{4}]^+$ to $[\mathbf{3}]^{2+}$ and $[\mathbf{4}]^{2+}$ in MeCN is owed to substantial thermodynamic stabilization of the dicationic species $[\mathbf{3}]^{2+}$ and $[\mathbf{4}]^{2+}$ by MeCN coordination to the metals (in good agreement with the disproportionation reactivity of $[\mathbf{3}]^+$ and $[\mathbf{4}]^+$ in MeCN described below).

Synthesis and characterization of the metallo-radicals $[\mathbf{3}]^+$ and $[\mathbf{4}]^+$: The low potentials for the oxidation of [{M(μ-az)(cod)}$_2$] (M = Rh, **3**; Ir, **4**), in both dichloromethane and acetonitrile suggest that the formation of the cationic compounds [{M(μ-az)(cod)}$_2$]$^+$ (M = Rh, $[\mathbf{3}]^+$; Ir, $[\mathbf{4}]^+$) should be readily achieved with mild chemical oxidants. With this in mind $[\mathrm{FeCp_2}]\mathrm{PF_6}$ was chosen as oxidant. In agreement with the above CV results, different results were obtained in $\mathrm{CH_2Cl_2}$ and in MeCN solvents. The reactions in dichloromethane and acetonitrile are described separately below.

After addition of one molar equivalent of $[\mathrm{FeCp_2}]\mathrm{PF_6}$ to a solution of complexes **3** and **4** in dichloromethane, the ^{1}H NMR spectra showed the immediate disappearance of the starting materials and the simultaneous appearance of broad resonances at unusual chemical shifts. This is a clear indication of quantitative formation of the paramagnetic compounds $[\mathbf{3}]^+$ and $[\mathbf{4}]^+$. After layering both solutions with diethyl ether, single crystals of $[\mathbf{3}]\mathrm{PF_6}$ and $[\mathbf{4}]\mathrm{PF_6}$, suitable for X-ray diffraction studies, were obtained. The structure of one of the independent cations $[\mathbf{3}]^+$ is shown in Figure 6 (for the isostructural complex $[\mathbf{4}]\mathrm{PF_6}$ see the Supporting Information) and selected bond lengths and angles are given in Table 3 (the data of the second independent molecule within brackets). The data for complex $[\mathbf{4}]\mathrm{PF_6}$ are included in Table 3 for comparison.

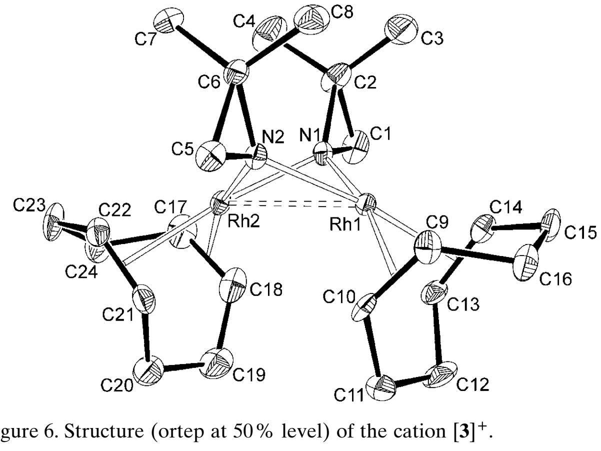

Figure 6. Structure (ortep at 50% level) of the cation $[\mathbf{3}]^+$.

Both structures are quite similar, and not very different from the structure of the precursor complex **3**. Removal of one electron in **3** and **4** strengthens the M−M interaction, as indicated by the shortening of the intermetallic distance by about 0.1 Å in $[\mathbf{3}]^+$ relative to the related neutral precursor **3**. The second relevant difference upon oxidation of complex **3** is the elongation of the Rh−C distances by about 0.06 Å.

Table 3. Selected bond lengths [Å] and angles [°] for $[\mathbf{3}]^+$ and $[\mathbf{4}]^+$.

	M = Rh ($[\mathbf{3}]^+$)[a]		M = Ir ($[\mathbf{4}]^+$)
M1−M2	2.6698(7)	[2.6781(7)]	2.6840(5)
M1−N1	2.035(5)	[2.042(5)]	2.050(8)
M1−N2	2.055(5)	[2.048(5)]	2.057(7)
M2−N1	2.038(5)	[2.049(5)]	2.056(8)
M2−N2	2.057(6)	[2.030(5)]	2.053(7)
M−Ct1[b]	2.066(8)	[2.067(8)]	2.036(14)
M1−Ct2[b]	2.059(7)	[2.066(8)]	2.038(11)
M2−Ct3[b]	2.056(8)	[2.070(8)]	2.034(10)
M2−Ct4[b]	2.067(8)	[2.044(7)]	2.046(12)
N1-M1-N2	80.4(2)	[80.5(2)]	78.4(3)
N1-M2-N2	80.3(2)	[80.7(2)]	78.3(3)
N1-M1-Ct1[b]	169.6(3)	[173.4(3)]	170.1(4)
N1-M1-Ct2[b]	95.9(3)	[95.4(3)]	96.0(4)
N1-M2-Ct3[b]	95.3(3)	[96.5(3)]	96.0(4)
N1-M2-Ct4[b]	172.2(3)	[167.3(3)]	170.4(4)
M1-N1-M2	81.9(2)	[81.8(2)]	81.7(3)
M1-N2-M2	81.0(2)	[82.12(19)]	81.5(3)

[a] Data of the second independent cation of $[\mathbf{3}]^+$ are shown in square brackets. [b] Ct1, Ct2, Ct3 and Ct4 are the midpoints between C9−C10, C13−C14, C17−C18, and C21−C22, respectively.

EPR spectroscopy and electronic structures of [3]$^+$ and [4]$^+$: The EPR spectra recorded at 20 K for the radicals $[\mathbf{3}]^+$ and $[\mathbf{4}]^+$, generated in situ by reacting complexes **3** and **4** with one molar equivalent $[FeCp_2]PF_6$ in acetone is shown in Figure 7. To improve the quality of the spectra, $n\mathrm{Bu_4NPF_6}$ (around 0.1 M) was added. The simulated spectra were generated by using the "best fit" spectral parameters listed in Table 4.

Simulation of the apparent axial spectrum of rhodium complex $[\mathbf{3}]^+$ (Figure 7, top) revealed that the species actually has a slightly rhombic g-tensor (Table 4). Hyperfine interaction (HFI) with two equivalent Rh nuclei (65 MHz) is resolved along $g_{33}(z)$. The DFT calculated Euler angles of the two equivalent A_{Rh}-tensors with respect to the g-tensor were applied in the spectral simulation, but simulation with coinciding interaction tensors (same principle axes) gave almost identical results. The spectrum of $[\mathbf{3}]^+$ reveals no resolved superhyperfine interactions with the nitrogen nuclei or any other nucleus.

The spectrum of iridium complex $[\mathbf{4}]^+$ is more complicated, and attempts to simulate the spectrum without contributions from the large nuclear quadrupole interactions (NQI) of iridium did not lead to satisfactory results. In EPR powder simulations of spectra from quadrupolar first- and second-row transition metals, the quadrupole interaction term $I_{\mathrm{Ir}}{\cdot}P{\cdot}I_{\mathrm{Ir}}$ is usually neglected in the spin Hamiltonian, because it contributes only marginally to the spectral fine structure. For iridium, however, the NQI is comparable to the iridium HFI and therefore this approximation is no longer valid. The "quadrupole effect" causes shifts and intensity redistributions within the HFI multiplet, so that these multiplets are no longer equally spaced. The NQI can also cause the appearance of "forbidden" ($\Delta m_I = 2$) transitions.[16,17,18] These effects severely complicated the spectral simulation of $[\mathbf{4}]^+$. "Easy approach" attempts to simulate the spectrum of $[\mathbf{4}]^+$, such as assuming all interaction ten-

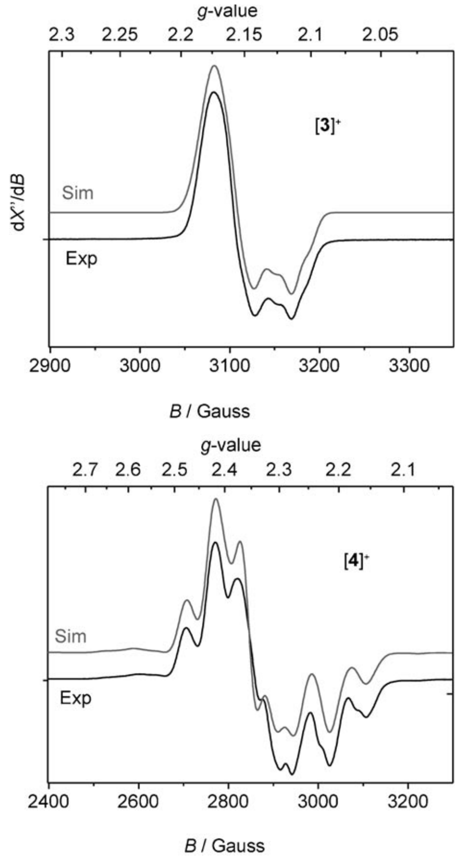

Figure 7. Experimental and simulated X-band EPR spectra of $[\mathbf{3}]^+$ (top) and $[\mathbf{4}]^+$ (bottom). Experimental conditions: $T = 20$ K, attenuation = 30 dB, field modulation amplitude = 4 Gauss, $\tilde{\nu} = 9.377282$ GHz for $[\mathbf{3}]^+$ (top) and 9.277588 GHz for $[\mathbf{4}]^+$ (bottom). The simulated spectra were obtained with the parameters given in Table 4.

Table 4. Experimental and DFT calculated EPR parameters of $[\mathbf{3}]^+$ and $[\mathbf{4}]^+$.

	Complex $[\mathbf{3}]^+$		Complex $[\mathbf{4}]^+$	
	Exp[a]	(*calc*)[b]	Exp[a]	(*calc*)[b]
g_{11}	2.171	(*2.194*)	2.418	(*2.486*)
g_{22}	2.159	(*2.174*)	2.350	(*2.314*)
g_{33}	2.115	(*2.100*)	2.212	(*2.154*)
$A^{\mathrm{M}}{}_{11}$	NR[e]	(*−35.3*)	145	(*112*)
$A^{\mathrm{M}}{}_{22}$	NR[e]	(*−50.8*)	88	(*127*)
$A^{\mathrm{M}}{}_{33}$	−65.0	(*−70.1*)	127	(*147*)
Euler angles A^{M}	0, 45, 0	(*0, 45, 0*)	0, 13, 0	(*−2, 42, 2*)
η[c]		(*2×39.7 %*)		(*2×43.4 %*)
$P^{\mathrm{Ir}}{}_{11}$[d]			−17	(*−108*)
$P^{\mathrm{Ir}}{}_{22}$			−164	(*−50*)
$P^{\mathrm{Ir}}{}_{33}$			181	(*158*)
Euler angles P^{Ir}			44, 38, −13	(*−2, 38, −2*)
$A^{\mathrm{N}}{}_{11}$	NR[e]	(*−1.9*)	NR[e]	(*−1.3*)
$A^{\mathrm{N}}{}_{22}$	NR[e]	(*−1.7*)	NR[e]	(*−1.0*)
$A^{\mathrm{N}}{}_{33}$	NR[e]	(*−10.8*)	NR[e]	(*−6.9*)
Euler angles A^{N}		(*−34, 88, −2*)		(*−32, 92, 91*)
η[c]		(*2×10.5 %*)		(*2×6.9 %*)

[a] Parameters from spectral simulations, [b] DFT calculated parameters (ADF, BP86/TZP), [c] Mulliken spin density population (ADF, BP86/TZP), [d] NQI tensor, [e] Not resolved in the experimental X-band EPR spectra.

Table 5. Selected bond lengths [Å] and angles [°] of the DFT optimized geometries of **3**, [**3**]$^+$, **4** and [**4**]$^+$.

	3 (M=Rh)	[**3**]$^+$ (M=Rh)	**4** (M=Ir)	[**4**]$^+$ (M=Ir)
M1 M2	2.871	2.767	2.924	2.814
M1−N1	2.130	2.088	2.146	2.111
M1−N2	2.131	2.086	2.149	2.111
M2−N1	2.132	2.086	2.150	2.112
M2−N2	2.131	2.088	2.146	2.111
M1−Ct1[a]	2.054	2.135	2.046	2.105
M1−Ct2[a]	2.055	2.129	2.047	2.102
M2−Ct3[a]	2.054	2.129	2.048	2.102
M2−Ct4[a]	2.053	2.134	2.045	2.105
N1-M1-N2	77.22	79.07	76.37	78.31
N1-M2-N2	77.20	79.06	76.36	78.29
N1-M1-Ct1[a]	97.71	97.60	98.27	97.78
N1-M1-Ct2[a]	169.69	169.50	169.75	169.24
N1-M2-Ct3[a]	97.52	97.26	98.09	97.58
N1-M2-Ct4[a]	173.56	173.46	173.09	173.09
M1-N1-M2	84.70	83.03	85.80	83.56
M1-N2-M2	84.71	83.04	85.81	83.59

[a] Ct1, Ct2, Ct3 and Ct4 are the midpoints between C9-C10, C13-C14, C17-C18 and C21-C22, respectively.

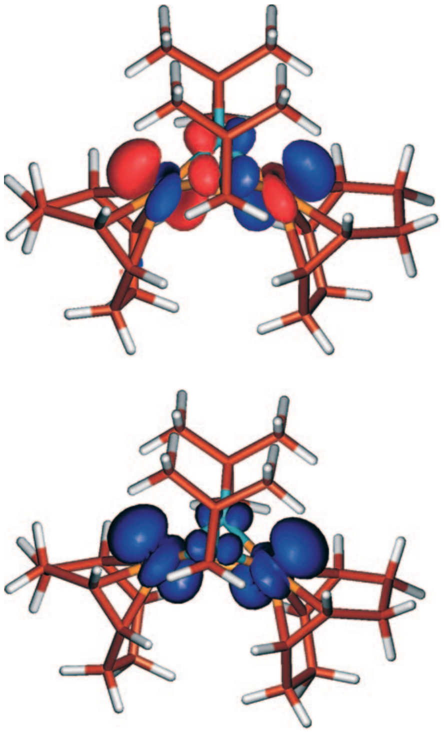

Figure 8. SOMO (top) and spin density (bottom) plots of [**4**]$^+$. The SOMO and spin density distribution of [**3**]$^+$ are almost identical.

sors to coincide (same principle axes) or by using Euler angles obtained from DFT EPR property calculations (vide infra), did not lead to any satisfactory results. Only by trial-and-error approaches (i.e. systematic variation of the *g*-, *A*- and *P*-tensors, their respective Euler angles and the line widths), we succeeded in obtaining a satisfactory simulation (Figure 7, bottom). From this simulation it is clear that rhombic spectrum of [**4**]$^+$ is dominated by iridium hyperfine and quadrupole interactions (Table 4).[19]

As expected for heavier transition metals with larger spin-orbit couplings, the *g*-anisotropy of the iridium complex is larger than that of the rhodium complex. The iridium HFI's are also larger than the rhodium HFI's. For both complexes the agreement between the experimental and the DFT calculated principle g-values is remarkably good. The HFI terms of rhodium complex [**3**]$^+$ are also predicted well by the DFT calculations. Assuming that the simulation in Figure 7 (bottom) represents a unique fit of the experimental data, the HFI and NQI terms of iridium complex [**4**]$^+$ are predicted less well by the DFT calculations.[19] The agreement between the principle values is reasonable, but the calculated Euler angles, especially those belonging to the NQI *P*-tensor, clearly deviate from the experimental ones. Apart from that, the DFT calculated EPR properties represent the experimental data quite well.

For both complexes, DFT spin density plots (turbomole) reveal that the unpaired electron is delocalized over the two metal centers and the two aziridinato N-donors, but it is mainly residing at the two metal centers (Figure 8). Mulliken spin-density populations from the ADF calculations at these nuclei are included in Table 4.

The relatively small spin-density populations of the N-donors (7–11 % per nitrogen nucleus) accounts for absence of resolved nitrogen HFI's in the EPR spectra. The spin-density populations at the metal centers are much larger (40–43 % per metal nucleus). The SOMO of the complexes is mainly built from two metal d-orbitals in an antibonding combination. Two aziridinato nitrogen p-orbitals contribute to the SOMO with smaller coefficients (Figure 8). Similar orbital interactions build the HOMO of the neutral complexes **3** and **4**, where occupation of this molecular orbital with two electrons makes the Rh−Rh interaction essentially repulsive.

Removal of one electron from the HOMO of **3** and **4** to obtain the SOMO of [**3**]$^+$ and [**4**]$^+$ leads to an increased metal−metal bond order, and thus a shortening of the M−M bonds. As expected, and in good agreement with the experimental structures, the M−N bond lengths become shorter, whereas the M-olefin interactions become weaker upon oxidation of **3** and **4** to [**3**]$^+$ and [**4**]$^+$, respectively. Selected calculated bond lengths of **3**, [**3**]$^+$, **4** and [**4**]$^+$ are shown in Table 5.

Reactivity of the metallo-radicals [3]$^+$ and [4]$^+$: Notably, the quite similar radicals [**3**]$^+$ and [**4**]$^+$ have remarkably different thermal stabilities in dichloromethane. The rhodium compound [**3**]$^+$ is stable in CH_2Cl_2 for days, and solid [**3**]PF_6 was obtained in very good yields after crystallization, whereas only few microcrystals of the iridium counterpart [**4**]PF_6 could be isolated. Monitoring the change of [**4**]PF_6 in dichloromethane by NMR spectroscopy, sharp resonances corresponding to diamagnetic products were observed to rise slowly. The transformation of [**4**]PF_6 was quantitative in 36 h, and the products were found to be the allyl complex $[(\eta^3,\eta^2\text{-}C_8H_{11})Ir(\mu\text{-az})_2Ir(cod)]PF_6$ ([**5**]PF_6) and the hydride compound [(cod)(H)Ir(μ-az)$_2$Ir(cod)]PF$_6$ ([**6**]PF$_6$) (Scheme 4), formed in equimolar amounts.

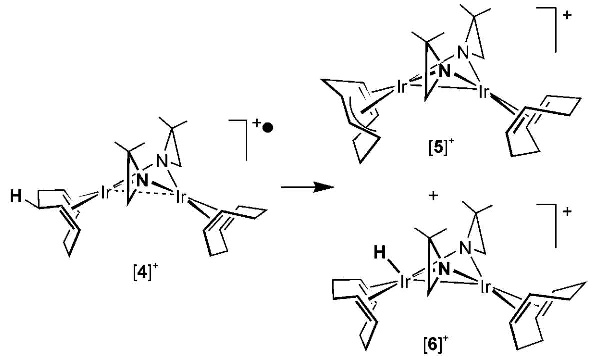

Scheme 4. Transformation of radical species [**4**]$^+$ in dichloromethane to form [**5**]$^+$ and [**6**]$^+$.

The allyl compound [(η^3,η^2-C_8H_{11})Ir(μ-az)$_2$Ir(cod)]PF$_6$ ([**5**]PF$_6$) was isolated as a purple crystalline solid after several fractional crystallizations from dichloromethane/diethyl ether. The allyl fragment of the η^3,η^2-cyclooctadienyl ligand was easily identified from its spectroscopic features (see the Experimental Section). The most relevant resonance was the triplet at $\delta = 3.16$ ppm corresponding to the central allylic proton, which was found to be coupled with two signals at $\delta = 5.68$ and 5.22 ppm, while the intact cod ligand showed the expected twelve signals in the ^{1}H NMR spectrum.

In addition, four methyl groups from the aziridinato ligands, according to the lack of symmetry in [**5**]PF$_6$, were easily identified. Moreover, complex [**5**]PF$_6$ was obtained as a single species with the stereochemistry depicted in Scheme 4, according to the NOESY spectrum. Therefore, from the eight allylic-cod protons just one of the four placed outside of the pocket of the complex (marked in Scheme 4) undergoes this allylic activation.

The hydride complex [(cod)(H)Ir(μ-az)$_2$Ir(cod)]$^+$ ([**6**]$^+$) was identified by comparison of its spectroscopic features with that of pure samples obtained by alternative methods. Thus, [**6**]BF$_4$ was easily prepared as a brown solid by reacting [{Ir(μ-az)(cod)}$_2$] (**4**) with HBF$_4$ in diethyl ether. The hydride ligand was easily located as a singlet at $\delta = -25.29$ ppm in the ^{1}H NMR spectrum of the complex, which was found to be stable in solution for weeks. There is exclusive protonation at the metal even in the presence of amido ligands in **4**. Moreover, it is remarkable that **3** and **4** can be handled and stored for months in the air without observing decomposition/hydrolysis, whereas the related bis(amido)complexes are, in our experience, easily hydrolyzed in the presence of traces of water.[5d]

For comparative purposes, we carried out the protonation of the previously reported complex [{Ir(cod)(μ-NHC$_6$H$_4$-Me)}$_2$] derived from *p*-toluidine. In this case, the reaction required two molar equivalents of HBF$_4$ to go to completion and, in spite of the less basic character of *p*-toluidine compared to dimethylaziridine, both amido ligands were protonated. The product was found to be the mononuclear η^5-aryl compound [Ir(cod){η^5-(H$_2$NC$_6$H$_4$-Me)}]BF$_4$ ([**7**]BF$_4$) whose structure is drawn in Figure 9 (for selected bond lengths and angles, see the Supporting Information).

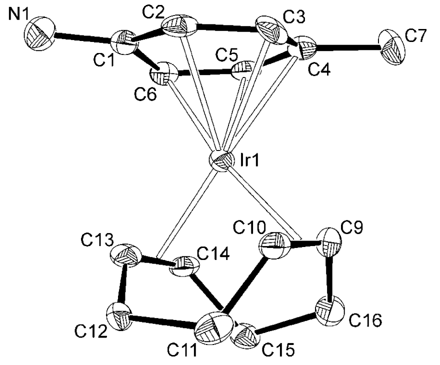

Figure 9. Structure (ortep at 50% level) of cation [**7**]$^+$.

Thus, compared to related amido-bridged species, the stability of the metal–nitrogen bonds of the bis(μ-aziridinato) compounds **3** and **4** is remarkable, resisting moisture and air in the solid state and in solution, and for which even reaction with strong acids such as HBF$_4$ does not lead to protonation of the amido fragment in case of **4**. The remarkable inertness of the metal-amido nitrogen bonds of **3** and **4** is likely the result of the special binding modes of the aziridinato ligands through 3c-4e interactions, as depicted in Figure 3.

Addition of ligands, such as acetonitrile, to dichloromethane solutions of [**6**]PF$_6$ did not lead to insertion of hydride into the metal-olefin bond, neither to hydrogen transfer to the neighboring nitrogen atom to form aziridine. Nevertheless, solutions of complex [**6**]PF$_6$ in [D$_6$]acetone show a slow disappearance of the resonance corresponding to the hydride due to an exchange with deuterium. The acidic character of this hydride in complex [**6**]$^+$ is clearly shown by the quantitative transformation into complex **4** by treatment with hexamethyltetraamine (hmta). More interesting, the reaction between [**6**]$^+$ and TEMPO$^\bullet$ (1:1 molar ratio) resulted in the quantitative formation of the radical [**4**]$^+$ and TEMPO-H, indicating that [**6**]$^+$ is not only a carrier for protons but also for radicals H$^\bullet$. In other words, the Ir–H bond in [**6**]$^+$ can be cleaved in a homolytic or heterolytic way, depending on the reagent employed.

Formation of the M^{III}(η^3,η^2-C_8H_{11}) (M = Rh, Ir) moieties from typical 1,5-cyclooctadiene (cod) complexes [M^I(η^2,η^2-C_8H_{12})], although still rare, has been previously observed for mononuclear anionic complexes of the type [M(cod)(η^5-L)]$^-$ (L = $C_2B_9H_9Me_2$,[20] $C_2B_9H_9Ph_2$,[21] Cp ligands[22]), mononuclear cationic compounds with P-based[23] and N-based ligands,[24] whereas the chloride[25] and pyrazolate[26] bridged complexes are the single examples for dinuclear complexes.

The panoramic picture on this reaction, and the conditions to achieve it, still remain quite elusive. On one hand, a typical allylic C–H activation reaction promoted by a diamagnetic M^I center is the commonly accepted first step of the reaction, which can be followed by spontaneous[21] or deliberate H^- abstraction (with $[CPh_3]BF_4$)[20] (path a, Scheme 5), insertion into an alkyne present in the reaction medium[23a,26] (path b, Scheme 5) or a reductive-elimination reaction (path c, Scheme 5).[25] In other instances, a preactivation process is required which, in general, corresponds to an oxidation reaction as that reported by Togni[23b] with iodine (path d, Scheme 5) or after the neat transfer of one electron described by Green[22] and de Bruin[24] (path e, Scheme 5). For the dicationic metallo-radicals $[Ir^{II}(cod)(N\text{-}ligand)]^{2+}$ derived from poly(picolyl)amines,[24] a direct hydrogen-atom abstraction from an allylic C–H bond by another metallo-radical has been proposed to account for the simultaneous formation of the "$Ir^{III}(\eta^3,\eta^2\text{-}C_8H_{11})$" and "$Ir^{III}(H)(cod)$" moieties (Scheme 5). Several points of evidence were gathered in favor of a direct hydrogen atom abstraction from an allylic position of one species by the metal of another. The electrochemical data revealed $\Delta G^{\neq}_{disp}$ values for disproportionation larger than 29 kcal mol^{-1} for the fastest reacting species, reacting even at −80 °C, and the species revealing lower $\Delta G^{\neq}_{disp}$ values were shown to react much slower. Thus, it is very improbable that the reaction would proceed through initial electron transfer disproportionation. The reaction was shown to be 2nd order in Ir, and the complexes with the least steric bulk around the metal react much faster than the ones being more open. Furthermore, those reactions were shown to be accelerated by H^+, which speaks against a reversible disproportionation equilibrium followed by a rate limiting deprotonation of $\{Ir^{III}(cod)\}$ to $\{Ir^{III}(allyl)\}$.

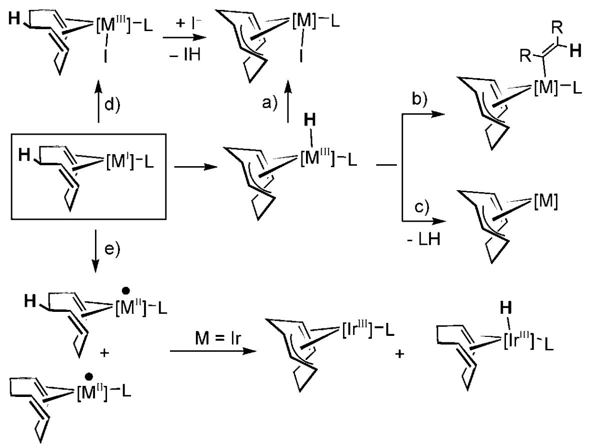

Scheme 5. Proposed mechanisms for the formation of "$M(\eta^3,\eta^2\text{-}C_8H_{11})$" moieties. a) Allylic activation followed by hydride abstraction. b) Allylic activation followed by alkyne insertion. c) Allylic activation followed by reductive elimination. d) Two-electron oxidation by iodine followed by allylic deprotonation. e) One-electron oxidation followed by binuclear H-transfer.

In case of $[\mathbf{4}]^+$, however, the situation could well be different. First of all, the disproportionation is less unfavorable for $[\mathbf{4}]^+$, presumably owed to the 1+ charge instead of a 2+ charge. The ΔG^0_{disp} value for disproportionation of $[\mathbf{4}]^+$ to **4** and $[\mathbf{4}]^{2+}$ derived from the electrochemical data amounts to 21 kcal mol^{-1}. Therefore, the activation barrier for disproportionation must be $\Delta G^{\neq}_{disp} > 21$ kcal mol^{-1}. Although substantial, this value is very close to that expected for a very slow reaction in solution at room temperature (taking 36 h to be complete). The Rh analog $[\mathbf{3}]^+$ has a larger $\Delta G^{\neq}_{disp}$ value of at least +23 kcal mol^{-1}. This could be sufficient to prevent the reaction to occur at an appreciable rate at room temperature. Furthermore, the oxidation of Ir complex $[\mathbf{4}]^+$ to $[\mathbf{4}]^{2+}$ is associated with a clearly detectable follow-up chemical reaction in the CV measurements, whereas oxidation of the Rh analog $[\mathbf{3}]^+$ to $[\mathbf{3}]^{2+}$ is completely reversible. The EC mechanism observed for oxidation of $[\mathbf{4}]^+$ most appreciably involves cod deprotonation after oxidation to $[\mathbf{4}]^{2+}$. Apparently, the cod protons of $[\mathbf{4}]^{2+}$ are more acidic than those of $[\mathbf{3}]^{2+}$, owing to stronger metal olefin interactions to Ir^{III} compared to Rh^{III}. The electrochemical data are thus strongly in favor of a mechanism in which two species $[\mathbf{4}]^+$ disproportionate to form **4** and $[\mathbf{4}]^{2+}$, followed by deprotonation of $[\mathbf{4}]^{2+}$ at an allylic position of its cod fragment to form the allyl species $[\mathbf{5}]^+$, after which the proton ends-up at the metal of **4** to form hydride species $[\mathbf{6}]^+$ (Scheme 6). A space filling CPK model of $[\mathbf{4}]^+$ also indicates that a direct metal-centered hydrogen-abstraction is severely hindered by the ancillary ligands, which is in favor of a preceding outer-sphere electron transfer disproportionation reaction.

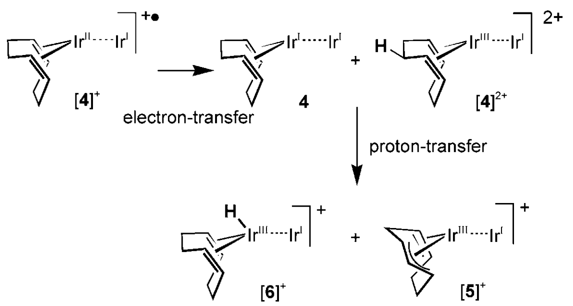

Scheme 6. Proposed mechanism for the formation of complexes $[\mathbf{5}]^+$ and $[\mathbf{6}]^+$.

According to the cyclic-voltammograms of complexes **3** and **4** in acetonitrile described above, addition of small amounts of acetonitrile to freshly prepared dichloromethane solutions of the metallo-radicals $[\mathbf{3}]^+$ and $[\mathbf{4}]^+$ triggers an immediate disproportionation reaction to equimolecular amounts of the starting materials **3** and **4** and metal-bonded M^{II}–M^{II} complexes.

The coupled chemical reaction associated to the oxidation process, envisaged by CV, was found to be the decoordination of one of the cod ligands and the incorporation of four molecules of acetonitrile to the dinuclear entity to produce the dicationic compounds $[(MeNC)_3M(\mu\text{-az})_2M(NCMe)(cod)](PF_6)_2$ (M = Rh $[\mathbf{8}](PF_6)_2$; Ir, $[\mathbf{9}](PF_6)_2$) (Scheme 7). Most logically, the first steps towards the formation of $[\mathbf{8}]^{2+}$ and $[\mathbf{9}]^{2+}$ will be the coordination of MeCN (Scheme 3),

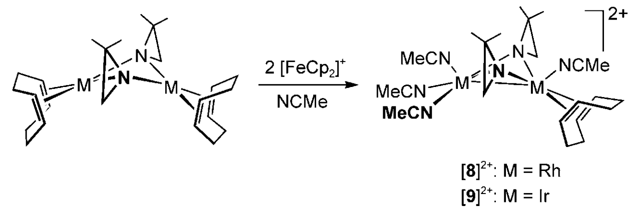

Scheme 7. Synthesis of the dicationic complexes [**8**]$(PF_6)_2$ and [**9**]$(PF_6)_2$.

after which apparently only one of the two cod fragments dissociates. On a preparative scale, both complexes were prepared in good yields by reacting **3** and **4** with two molar equivalents of $[FeCp_2]PF_6$ in acetonitrile.

Both complexes have been fully characterized, including a X-ray crystallographic study on complex [**9**]$(PF_6)_2$. The molecular structure of dicationic [**9**]$^{2+}$ is shown in Figure 10 while selected distances and angles are given in Table 6.

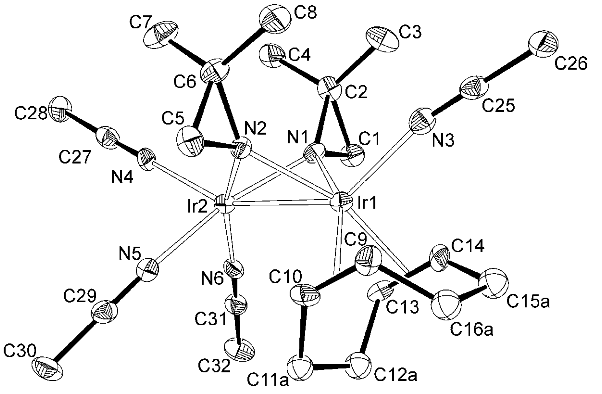

Figure 10. Structure (ortep at 50% level) of the dicationic complex [**9**]$^{2+}$.

Table 6. Selected bond lengths [Å] and angles [°] for complex [**9**]$^{2+}$.

Ir1–N1	2.100(6)	Ir2–N1	2.026(6)
Ir1–N2	2.085(5)	Ir2–N2	2.008(6)
Ir1–N3	2.157(6)	Ir2–N4	2.070(6)
Ir1–Ct1[a]	2.038(8)	Ir2–N5	2.028(6)
Ir1–Ct2[a]	2.049(7)	Ir2–N6	2.034(6)
N1-Ir1-N2	76.0(2)	N1-Ir2-N2	79.4(2)
N1-Ir1-N3	100.4(2)	N1-Ir2-N4	108.5(2)
N2-Ir1-N3	100.8(2)	N2-Ir2-N4	110.5(2)
N4-Ir2-Ir1	154.50(16)	N3-Ir1-Ir2	139.62(16)
N1-Ir1-Ct1[a]	159.3(3)	N1-Ir2-N5	165.1(2)
N2-Ir1-Ct2[a]	158.1(2)	N2-Ir2-N6	163.8(2)
Ct1-Ir1-Ct2	86.0(3)	N5-Ir2-N6	88.5(2)

[a] Ct1 and Ct2 are the midpoints between C9-C10 and C13-C14, respectively.

The overall geometry of [**9**]$^{2+}$ may be described roughly as formed by two square pyramids sharing an edge of the bases, in such a way that the environment of one metal can be considered distorted octahedral if the other metal occupies the sixth position of coordination. Each Ir center shares the nitrogen atoms of two *cis*-aziridinato ligands and the apex of each pyramid is occupied by the nitrogen of one acetonitrile ligand. In addition, the Ir1 atom completes its coordination environment with a chelating cyclooactadiene, whereas Ir2 completes its coordination environment with two additional acetonitrile ligands. The short separation between the iridium atoms, 2.5418(4) Å, indicates that they are linked by a metal–metal bond, and accordingly the M–M antibonding orbital, similar to that of the SOMO of complex [**4**]$^+$, is empty. The longer Ir–N bond lengths in the apical positions can be explained by the *trans*-influence of the metal–metal bond, or due to the antibonding character in these apical bonds of the HOMO.[8a]

The structure found in the solid state for complex [**9**]$^{2+}$ is maintained in solution for both complexes, according to the NMR spectra. Thus, two non-equivalent faces of the bridging aziridinato ligands (pointing at the "M(cod)(CH_3CN)" and "M$(CH_3CN)_3$" moieties, respectively) were deduced by the two signals of the methyl groups in the ^{1}H NMR spectrum. According to the structure, two coupled olefin signals are observed, as expected from the folded conformation of the M_2N_2 ring and of the symmetry plane of the cation. The acetonitrile ligands in the "M$(CH_3CN)_3$" moiety in the rhodium complex [**8**]$^{2+}$ are labile, as they undergo a fast exchange with the deuterated acetonitrile solvent, whereas those in the iridium complex [**9**]$^{2+}$ remain coordinated. In both complexes, the acetonitrile in the "M(cod)(CH_3CN)" moiety is observed as a broad signal in the ^{1}H NMR spectra.

Conclusion

The amido-bridged complexes [{M(μ-az)(cod)}$_2$] (M = Rh, **3**; M = Ir, **4**) are unusually stable towards hydrolysis, and the metal–amido bonds even survive reactions with strong acids. This unusual inertness of the aziridinato metal–nitrogen bonds is ascribed to the unusual bridging bonding modes of the aziridinato ligands with the two metal centers, involving 3c-4e interactions for each aziridinato ligand. These interactions also explain the relative short intermetallic distance of these complexes. The electrochemical behavior of **3** and **4** is greatly influenced by the solvent. Chemical oxidation of **3** and **4** in CH_2Cl_2 gives the paramagnetic cationic species [{M(μ-az)(cod)}$_2$]$^+$ (M = Rh, [**3**]$^+$; M = Ir, [**4**]$^+$) resulting from one-electron oxidation. The electron is removed from the M–M d–d σ*-antibonding HOMO, resulting in stronger metal–metal interactions in [**3**]$^+$ and [**4**]$^+$. EPR measurements and DFT calculations are in good agreement, confirming that the unpaired electron is delocalized over the two metal centers, with minor spin densities at the two bridging amido nitrogen groups, and is the result of a delocalized M–M d–d σ*-antibonding SOMO. These dinuclear species, therefore, do not form aminyl radical complexes upon one electron oxidation. While Rh complex [**3**]$^+$ is stable in dichloromethane, the Ir complex [**4**]$^+$ transforms slowly, but quantitatively, into a 1:1 mixture of the allyl complex [(η^3,η^2-C_8H_{11})Ir(μ-az)$_2$Ir(cod)] ([**5**]$^+$) and the hydride compound [(cod)(H)Ir(μ-az)$_2$Ir(cod)] ([**6**]$^+$). The mechanism proposed for this reaction involves initial disproportionation of $[\mathbf{4}]^+$ to **4** and $[\mathbf{4}]^{2+}$ ($\Delta G^0 = +21\ \mathrm{kcal\,mol^{-1}}$) followed by proton transfer from $[\mathbf{4}]^{2+}$ to **4** to form $[\mathbf{5}]^+$ and $[\mathbf{6}]^+$. A similar disproportionation reaction of Rh complex $[\mathbf{3}]^+$ in CH_2Cl_2 is apparently too much uphill ($\Delta G^{\neq} > +23\ \mathrm{kcal\,mol^{-1}}$) to occur at an appreciable rate at room temperature. In accordance with the electrochemical studies, the addition of small amounts of acetonitrile to dichloromethane solutions of $[\mathbf{3}]^+$ and $[\mathbf{4}]^+$ triggers a fast disproportionation in both cases, leading to equimolecular amounts of the starting materials **3** and **4** and metal–metal bonded, mixed ligand M^{II}–M^{II} species.

Experimental Section

Starting materials and physical methods: All the operations were carried out under argon atmosphere by using standard Schlenk-tube techniques. Solvents were purified by standard procedures. 2,2-dimethylaziridine,[27] [{M(μ-OMe)(cod)}$_2$] (M = Rh, Ir),[28] and [FeCp$_2$][PF$_6$][29] were prepared according to the literature methods. HBF_4 (Aldrich, 54% w/w in Et_2O) was commercially available and was used as received. Elemental analyses were performed by using a Perkin–Elmer 2400 microanalyzer. Mass spectra (MALDI) were recorded with a Bruker MicroFlex spectrometer using DCTB (1,1-dicyano-4-*t*-butylphenyl-3-methylbutadiene) as matrix. NMR spectra were recorded by using a Bruker AV 300 and AV 500 operating at 300.13 and 500.13 MHz, respectively, for ^{1}H. Chemical shifts are referenced to $SiMe_4$. Electrochemical experiments were performed by means of an EG&G Research Model 273 potentiostat/galvanostat. A three-electrode glass cell consisting of a platinum-disk working electrode, a platinum-wire auxiliary electrode and a KCl saturated calomel reference (SCE) electrode was employed. Linear voltamperometry was performed by using a rotating platinum electrode (RDE) as the working electrode. The supporting electrolyte solution (NBu_4PF_6, 0.1 M) was scanned over the solvent window to ensure the absence of electroactives impurities curves. A concentration of the analyte of about 2.5 10^{-4} M was employed in all the measurements.

Synthesis of the complexes: **[{Rh(cod)}$_2$(μ-az)(μ-OMe)] (1)**: Neat 2,2-dimethylaziridine (Haz) (0.154 mL, 0.813 mmol) was added to a solution of [{Rh(μ-OMe)(cod)}$_2$] (100.0 mg, 0.413 mmol) in toluene (10 mL). The solution was stirred for 12 h at RT. Thereafter, the resulting solution was evaporated to dryness. The residue was dissolved in hexane and the resulting solution was kept at −18 °C overnight to allow a green microcrystalline solid to form, complex **1**. The mother liquor was decanted and the solid was dried under vacuum. Yield: 47.5 mg (44%); ^{1}H NMR (C_6D_6, 25 °C) (assigned from the ^{1}H,^{1}H-COSY spectrum): $\delta = 4.03$ (m, 2H), 3.86 (m, 2H) and 3.54 (m, 4H; HC=), 3.21 (s, 3H; OMe), 2.69 (m, 2H), 2.51 (m, 2H), 2.36 (m, 2H), 2.23 (m, 2H; H_2C^{exo}), 1.94–1.71 (m, 6H), 1.43 (m, 2H; H_2C^{endo}), 1,64 (s, 6H; *Me*$_2$CCH$_2$N), 0.68 ppm (s, 2H; Me$_2$CC*H*$_2$N); ^{13}C{^{1}H} NMR (C_6D_6, 25 °C): $\delta = 82.1$ (d, J(C,Rh) = 12.1 Hz), 80.2 (d, J(C,Rh) = 11.7 Hz), 73.7 (d, J(C,Rh) = 14.8 Hz), 72.6 (d, J(C,Rh) = 15.1 Hz) (HC=), 55.0 (OMe), 40.2 (Me$_2$CC*H*$_2$N), 32.7, 31.4, 30.9 and 30.9 (H_2C), 32.1 (Me$_2$*C*CH$_2$N), 29.3 ppm (*Me*$_2$CCH$_2$N); elemental analysis calcd (%) for $C_{21}H_{35}NORh_2$ (523.3): C 48.20, H 6.74, N 2.68; found: C 48.08, H 6.40, N 2.66.

[{Ir(cod)}$_2$(μ-az)(μ-OMe)] (2): Complex **2** was prepared, as reported for **1**, starting from [{Ir(μ-OMe)(cod)}$_2$] (100.0 mg, 0.106 mmol) and Haz (0.120 mL, 0.633 mmol) to render orange microcrystals suitable for X-ray diffraction studies. Yield: 38 mg (36%); ^{1}H NMR (C_6D_6, 25 °C) (assigned from the ^{1}H,^{1}H-COSY spectrum): $\delta = 3.74$ (m, 2H), 3.62 (m, 2H), 3.35 (m, 2H), 2.68 (m, 2H; HC=), 3.62 (s, 3H; OMe), 2.27 (m, 4H), 2.17 (m, 2H), 2.07 (m, 2H; H_2C^{exo}), 1.67 (m, 2H), 1.55 (m, 6H; H_2C^{endo}), 1.51 (s, 6H; *Me*$_2$CCH$_2$N), 1.29 ppm (s, 2H; Me$_2$CC*H*$_2$N); ^{13}C{^{1}H} NMR (C_6D_6, 25 °C): $\delta = 65.2$, 63.7, 55.3, and 54.1 (HC=), 56.6 (OMe), 44.4 (Me$_2$CCH$_2$N), 33.1, 32.3, 32.2, and 32.0 (H_2C), 32.7 (Me$_2$*C*CH$_2$N), 29.3 ppm (*Me*$_2$CCH$_2$N); elemental analysis calcd (%) for $C_{21}H_{35}NOIr_2$ (701.9): C 35.93, H 5.03, N 2.00; found: C 35.66, H 4.97, N 1.94.

[{Rh(μ-az)(cod)}$_2$] (3): To a solution of [{Rh(μ-OMe)(cod)}$_2$] (198.0 mg, 0.818 mmol) in toluene (10 mL), containing activated molecular sieves (5 Å), Haz (1.6 mL, 8.4 mmol) was added. The suspension was stirred at 80 °C for 21 h. The resulting deep orange solution was filtered off, partially evaporated (≈2 mL), and kept a −18 °C overnight to yield complex **3** as a deep orange microcrystalline solid. The mother liquor was decanted and the crystals were dried under vacuum. Yield: 163.6 mg (71%); ^{1}H NMR (C_6D_6, 25 °C): $\delta = 3.77$ (m, 4H), 3.01 (m, 4H; HC=), 2.62 (m, 4H), 2.23 (m, 4H; H_2C^{exo}), 1.86 (m, 8H; H_2C^{endo}), 1.52 (s, 12H; *Me*$_2$CCH$_2$N), 0.80 ppm (s, 4H; Me$_2$CC*H*$_2$N); ^{13}C{^{1}H} NMR (C_6D_6, 25 °C): $\delta = 80.0$ (d, J(C,Rh) = 13 Hz), 77.1 (d, J(C,Rh) = 13 Hz) (HC=), 40.3 (Me$_2$CCH$_2$N), 32.6 (Me$_2$*C*CH$_2$N), 31.5 and 31.4 (H_2C), 29.1 ppm (*Me*$_2$CCH$_2$N); elemental analysis calcd (%) for $C_{24}H_{40}N_2Rh_2$ (562,4): C 51.25, H 7.17, N 4.98; found: C 51.09, H 7.46, N 5.09.

[{Ir(μ-az)(cod)}$_2$] (4): Complex **4** was obtained as dark-purple crystals as described for **3** starting from [{Ir(μ-OMe)(cod)}$_2$] (200.0 mg, 0.301 mmol) and Haz (0.50 mL, 2.60 mmol). Yield: 174.2 mg (78%); ^{1}H NMR (C_6D_6, 25 °C): $\delta = 3.51$ (m, 4H), 2.90 (m, 4H; HC=), 2.35 (m, 4H), 2.20 (m, 4H; H_2C^{exo}), 1.82 (m, 4H), 1.60 (m, 4H; H_2C^{endo}), 1.52 (s, 12H; *Me*$_2$CCH$_2$N), 1.31 ppm (s, 4H; Me$_2$CC*H*$_2$N); ^{13}C{^{1}H} NMR (C_6D_6, 25 °C): $\delta = 63.0$, 61.3 (HC=), 44.5 (Me$_2$CCH$_2$N), 32.5 (Me$_2$*C*CH$_2$N), 31.5 and 32.4 (H_2C), 28.6 ppm (*Me*$_2$CCH$_2$N); elemental analysis calcd (%) for $C_{24}H_{40}N_2Ir_2$ (741.0): C 38.90, H 5.44, N 3.78; found: C 39.11, H 6.06, N 3.66.

[{Rh(μ-az)(cod)}$_2$]PF$_6$ ([3]PF$_6$): A solution of [{Rh(μ-az)(cod)}$_2$] (**3**) (112.6 mg, 0.200 mmol) in dichloromethane (5 mL) was treated with [FeCp$_2$]PF$_6$ (66.3 mg, 0.200 mmol). After stirring for 12 h, the solution was carefully layered with diethyl ether (15 mL) and kept undisturbed for three days. The mother liquor was decanted and the deposited crystals, suitable for X-ray analyses, were dried under vacuum. Yield: 120.0 mg (85%); ^{1}H NMR (CD_2Cl_2, 25 °C): $\delta = 27.9$, 8.77, 0.22, −3.55, −14.3 ppm; elemental analysis calcd (%) for $C_{24}H_{40}N_2Rh_2PF_6$ (707.4): C 40.75, H 5.70, N 3.96; found: C 40.54, H 5.60, N 4.00.

[(η^3,η^2-C$_8$H$_{11}$)Ir(μ-az)$_2$Ir(cod)]PF$_6$ ([5]PF$_6$): A solution of [{Ir(μ-az)(cod)}$_2$] (**4**) (148.0 mg, 0.200 mmol) in dichloromethane (5 mL) was treated with [FeCp$_2$]PF$_6$ (66.3 mg, 0.200 mmol). The reaction was monitored by ^{1}H NMR to observe the quantitative transformation of the intermediate [**4**]PF$_6$ (which gives broad signals at $\delta = 42$ and 21 ppm) into equimolar amounts of [**5**]PF$_6$ and [**6**]PF$_6$ in ≈36 h at 25 °C. A spectroscopic an analytically pure sample of [**5**]PF$_6$ was isolated as a purple solid after three recrystallizations of the reaction mixture in dichloromethane/diethyl ether. Yield: 46.0 mg (26% relative to the starting material).

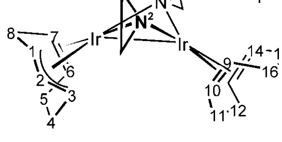

^{1}H (CD_2Cl_2, 25 °C): $\delta = 5.68$ (pseudo-q, 1H; H^1), 5.22 (pseudo-q, 1H; H^3), 4.37 (m, 1H; H^{14}), 4.11 (m, 2H; H^{6,9}), 3.72 (m, 1H; H^{10}), 3.53 (m, 1H; H^{13}), 3.45 (m, 1H; H^{4a}), 3.38 (m, 1H; H^{5a}), 3.16 (m, J(H,H) = 7.5 Hz, 1H; H^2), 2.67 (m, 1H; H^7), 2.59–2.35 (m, 7H; H^{4b,5b,8a,11a,11b,15a,16a}), 2.28 (m, 1H; H^{12a}), 2.17 (m, 2H; H^{12b,15b}), 2.12 (s, 1H; Me$_2$CC*H*$_2$N^1), 2.06 (s, 1H; Me$_2$CC*H*$_2$N^1), 1.95 (m, 1H; H^{16b}), 1.84 (s, 5H; *Me*$_2$CCH$_2$N^1 + Me$_2$CC*H*$_2$N^2), 1.53 (s, 3H; *Me*$_2$CCH$_2$N^1), 1.48 (s, 3H; *Me*$_2$CCH$_2$N^2), 1.45 (m, 1H; H^{8b}), 1.28 ppm (s, 3H; *Me*$_2$CCH$_2$N^2); ^{13}C{^{1}H} NMR (CD_2Cl_2, 25 °C): $\delta = 85.5$ (C^{14}), 85.1 (C^6), 82.5 (C^2), 81.0 (C^9), 78.3 (C^{10}), 74.4 (C^{13}), 69.0 (C^1), 48.7 and 47.7 (Me$_2$C*C*H$_2$N), 41.5 (C^5), 37.1 (Me$_2$*C*CH$_2$N^2), 35.8 (Me$_2$CCH$_2$N^1), 34.3 (C^{15}), 31.5 (C^7), 31.3 (C^{11}), 31.0 (C^{16}), 30.95 (C^3), 30.92 (*Me*$_2$CCH$_2$N^1), 29.0 (C^8), 28.2 (C^{12}), 27.6 (*Me*$_2$CCH$_2$N^2), 25.2 (*Me*$_2$CCH$_2$N^1), 25.1 (*Me*$_2$CCH$_2$N^2), 21.9 ppm (C^4); MS [m/z (%)]: 739.2

(100 %) M^+; elemental analysis calcd (%) for $C_{24}H_{39}N_2Ir_2PF_6$ (884.98): C 32.57, H 4.44, N 3.17; found: C 32.61, H 4.51, N 3.10.

[(cod)(H)Ir(μ-az)$_2$Ir(cod)]PF$_6$ ([6]PF$_6$): Addition of HBF_4 (29.3 μL, 54 % in Et_2O, 0.213 mmol) to a solution of [{Ir(μ-az)(cod)}$_2$] (**4**) (157.0 mg, 0.424 mmol) in diethyl ether (5 mL) produced the immediate precipitation of a brown solid. The solid was filtered, washed with diethyl ether (3×2 mL) and vacuum-dried. Yield: 162.4 mg (92 %).

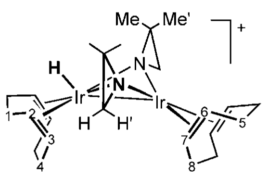

^{1}H NMR (CD_2Cl_2, 25 °C): $\delta = 4.44$ (m, 2H; H^7), 3.74 (m, 2H; H^6), 4.17 (m, 2H; H^3), 3.80 (m, 2H; H^2), 2.61 (m, 2H; H^{4a}), 2.55–2.25 (m, 12H; $H^{1a,1b,4b,5a,5b,8a}$), 2.04 (m, 4H; $CH + H^{8b}$), 1.67 (s, 2H; CH'), 1.52 (s, 6H; Me′), 1.48 (s, 6H; Me), −25.29 ppm (s, 1H; IrH); $^{13}C\{^1H\}$ NMR (CD_2Cl_2, 25 °C): $\delta = 83.8$ (C^3), 76.2 (C^2), 33.3 (C^1), 30.1 (C^4), 83.7 (C^7), 78.0 (C^6), 32.6 (C^8), 29.0 (C^5), 36.9 (CH_2), 32.2 (Me′), 23.2 ppm (Me); elemental analysis calcd (%) for $C_{24}H_{41}N_2Ir_2BF_4$ (828.83): C 34.78, H 4.99, N 3.38; found: C 34.87, H 4.91, N 3.19.

[Ir(cod)(η^5-{H$_2$NC$_6$H$_4$-Me}]BF$_4$ ([7]BF$_4$): A solution of [{Ir(cod)(μ-NHC_6H_4-Me)}$_2$] (90.0 mg, 0.11 mmol) in CH_2Cl_2 (5 mL) was treated with HBF_4 (30.3 μL, 0.22 mmol). After 4 h stirring, the resulting solution was concentrated to 2 mL and layered with Et_2O. After three days, the mother liquor was decanted and the crystals were dried under vacuum. Yield: 72.0 mg (66 %). ^{1}H NMR ($CDCl_3$, 25 °C): $\delta = 6.11$ (d, $J(H,H) = 6.6$ Hz, 2H; NC_6H_4Me), 6.04 (d, $J(H,H) = 6.6$ Hz, 2H; NC_6H_4Me), 5.45 (br, 2H; NH_2), 4.10 (m, 4H; HC=), 2.23 (s, 3H; NC_6H_4Me), 2.18 (m, 4H; H_2C^{exo}), 1.99 ppm (m, 4H; H_2C^{endo}); $^{13}C\{^1H\}$ NMR ($CDCl_3$, 25 °C): $\delta = 138.8$ (C^1), 108.0 (C^4), 94.7 (C^3), 76.4 (C^2) (NC_6H_4Me), 64.4 (HC=), 33.0 (CH_2), 18.1 ppm (NC_6H_4Me); MS [m/z (%)]: 408 (100 %) M^+; elemental analysis calcd (%) for $C_{15}H_{21}IrNBF_4$ (494.36): C 36.44, H 4.28, N 2.83; found: C 36.29, H 4.67, N 2.68.

[(MeNC)$_3$Rh(μ-az)$_2$Rh(NCMe)(cod)](PF$_6$)$_2$ [8](PF$_6$)$_2$: A suspension of [{Rh(μ-az)(cod)}$_2$] (**3**) (25.3 mg, 0.045 mmol) in CH_3CN (2 mL) was treated with [$FeCp_2$][PF_6] (30.1 mg, 0.09 mmol). After stirring for 3 h, the resulting brown-orange solution was evaporated to dryness. The residue was washed with diethyl ether (3×5 mL) to remove [$FeCp_2$] and recrystallized from acetonitrile/diethyl ether to render red-brown crystals, which were decanted and vacuum-dried. Yield: 32.1 mg (79 %). ^{1}H NMR (CD_3CN, 25 °C): $\delta = 4.60$ (br, 2H), 3.91 (br, 2H; HC=), 2.90 (m, 2H), 2.66 (m, 2H; H_2C^{exo}), 2.45 (m, 2H), 2.37 (m, 2H; H_2C^{endo}), 2.10 (br, 3H; CH_3CN), 1.99 (s, 9H; free MeCN), 1.50 (s, 6H), 1.33 (s, 6H; Me_2CCH_2N), 0.94 (br, 2H), 0.55 ppm (br, 2H; Me_2CCH_2N); $^{13}C\{^1H\}$ NMR (CD_3CN, 25 °C): $\delta = 105.4$ (d, $J(C,Rh) = 9$ Hz), 91.3 (d, $J(C,Rh) = 6$ Hz) (HC=), 41.6 (Me_2CCH_2N), 40.2 (Me_2CCH_2N), 31.9 and 28.5 (H_2C), 26.8 and 25.3 (Me_2CCH_2N), 3.62 ppm (m, $J(C,D) = 21$ Hz, 3C, $Rh(CD_3CN)_3$); elemental analysis calcd (%) for $C_{24}H_{40}N_6Rh_2P_2F_{12}$ (908.3): C, 31.73; H, 4.44; N, 9.25; found: C, 31.68; H, 4.30; N, 9.45.

[(MeNC)$_3$Ir(μ-az)$_2$Ir(NCMe)(cod)](PF$_6$)$_2$ [9](PF$_6$)$_2$: Complex **9** was obtained as red-yellow crystals as described for [**8**](PF_6)$_2$ starting from [{Ir(μ-az)(cod)}$_2$] (75.0 mg, 0.101 mmol) and [$FeCp_2$][PF_6] (66.8 mg, 0.202 mmol). Yield: 92.2 mg (84 %). ^{1}H NMR (CD_3CN, 25 °C): $\delta = 4.23$ (br, 2H), 3.56 (br, 2H; HC=), 2.70 (s, 9H; CH_3CN), 2.65 (m, 2H), 2.56 (m, 2H; H_2C^{exo}), 2.31 (m, 2H), 2.23 (m, 2H; H_2C^{endo}), 2.18 (br, 3H; CH_3CN), 1.46 (s, 6H), 1.35 (s, 6H; Me_2CCH_2N), 1.02 (br, 2H), 0.69 ppm (br, 2H; Me_2CCH_2N); $^{13}C\{^1H\}$ NMR (CD_3CN, 25 °C): $\delta = 84.9$ and 71.5 (HC=), 44.7 (Me_2CCH_2N), 40.7 (Me_2CCH_2N), 33.5 and 28.3 (H_2C), 26.4 and 24.2 (Me_2CCH_2N), 3.19 ppm ($Ir(CH_3CN)_3$); elemental analysis calcd (%) for $C_{24}H_{40}N_6Ir_2P_2F_{12}$ (1087.0): C, 26.52; H, 3.71; N, 7.73; found: C, 27.30; H, 3.36; N, 7.48.

EPR spectroscopy: Experimental X-band EPR spectra were recorded by using a Bruker EMX spectrometer equipped with a He temperature control cryostat system (Oxford Instruments). The spectra were simulated by iteration of the anisotropic *g* values, (super)hyperfine coupling constants, the iridium nuclear quadrupole tensor (complex $\mathbf{3}^+$), and line widths by using XSophe EPR simulation software (Bruker BioSpin Corporation). The spectra were simulated with the general spin Hamiltonian in Equation (1) with two equivalent nuclei:

$$\mathscr{H} = \beta B \cdot g \cdot S + S \cdot A \cdot I_M + S \cdot A \cdot I_N + I_M \cdot P \cdot I_M \quad (1)$$

Table 7. Selected crystallographic data of **2**, **3**, [**3**]PF_6, [**4**]PF_6, [**7**]BF_4 and [**9**](PF_6)$_2$·CH_2Cl_2.

	2	**3**	[**3**]PF_6	[**4**]PF_6	[**7**]BF_4	[**9**](PF_6)$_2$·CH_2Cl_2
formula	$C_{21}H_{35}Ir_2NO$	$C_{24}H_{40}N_2Rh_2$	$C_{24}H_{40}F_6N_2PRh_2$	$C_{24}H_{40}F_6Ir_2N_2P$	$C_{15}H_{21}BF_4IrN$	$C_{25}H_{42}Cl_2F_{12}Ir_2N_6P_2$
formula weight	701.90	562.40	707.37	885.95	494.34	1171.89
color	red	red-orange	red	red	red-orange	yellow
crystal system	tetragonal	orthorhombic	monoclinic	monoclinic	triclinic	monoclinic
space group	$P4_32_12$	$Fdd2$	$P2_1/c$	$P2_1/n$	$P\bar{1}$	$P2_1/c$
a [Å]	13.1713(8)	18.9524(15)	13.0695(9)	9.2913(7)	10.8446(14)	16.2592(11)
b [Å]	13.1713(8)	26.108(2)	24.2257(16)	23.8159(19)	12.6003(16)	8.8001(6)
c [Å]	23.7804(14)	9.2663(7)	17.8312(12)	12.7132(10)	12.8111(16)	27.2505(19)
α [°]	90	90	90	90	107.675(2)	90
β [°]	90	90	109.2360(10)	109.1510(10)	103.752(2)	106.3520(10)
γ [°]	90	90	90	90	102.441(2)	90
V [Å^3]	4125.5(4)	4585.0(6)	5330.5(6)	2657.5(4)	1539.9(3)	3741.4(4)
Z	8	8	8	4	4	4
$F(000)$	2640	2304	2856	1684	944	2240
ρ_{calcd} [g cm^{-3}]	2.260	1.629	1.763	2.214	2.132	2.080
μ [mm^{-1}]	12.898	1.452	1.357	10.124	8.706	7.422
crystal size [mm]	0.20×0.18×0.16	0.29×0.13×0.12	0.08×0.05×0.04	0.30×0.11×0.04	0.10×0.09×0.06	0.13×0.09×0.02
T [K]	293(2)	173(2)	100(2)	100(2)	100(2)	100(2)
θ limits [°]	1.77–27.00	2.57–28.00	1.47–26.00	1.71–26.00	1.76–27.00	1.56–26.00
collected reflns.	26345	13731	31420	15648	18202	39115
unique reflns (R_{int})	4510 (0.0406)	2735 (0.0436)	10466 (0.0623)	5228 (0.0358)	6671 (0.0456)	7344 (0.0691)
reflns with [$I > 2\sigma(I)$]	4257	2628	7936	4464	5473	6037
parameters/restraints	229/0	130/1	625/91	292/54	399/0	443/34
R_1 (on F, [$I > 2\sigma(I)$])	0.0233	0.0273	0.0575	0.0431	0.0407	0.0425
wR_2 (on F^2, all data)	0.0488	0.0628	0.1304	0.1118	0.0944	0.0910
Goodness-of-fit	1.039	1.104	1.025	1.021	1.019	1.086
max/min $\Delta\rho$ [e Å^{-3}]	0.760/−0.501	1.068/−0.477	1.843/−1.745	1.890/−1.378	2.558/−2.358	2.427/−1.629

DFT geometry optimizations and EPR parameter calculations: All geometry optimizations were carried out by means of the Turbomole program[30a] coupled to the PQS Baker optimizer.[31] Geometries were fully optimized as minima at the b3-lyp level[32] by using the Turbomole TZVP basis[30c,f] (small-core pseudopotential[30c,e] on Rh or Ir). EPR parameters[33] were calculated with the ADF[34] program system by using the bp86[35] functional with the ZORA/TZP basis set supplied with the program (all electron, core double zeta, valence triple zeta polarized basis set on all atoms), using the coordinates from the structures optimized in Turbomole as input. Orbital and spin density plots were generated with Molden.[36]

Structural analysis of 2, 3, [3]PF$_6$, [4]PF$_6$, [7]BF$_4$ and [9](PF$_6$)$_2$·CH$_2$Cl$_2$: X-ray data were collected by using a Bruker Smart Apex CCD diffractometer, with graphite-monochromated Mo$_{K\alpha}$ radiation ($\lambda = 0.71073$ Å) using ω scans (0.3°). Data were corrected for absorption using a multiscan method applied with SADABS program.[37] Selected crystallographic data can be found in Table 7. The structures were solved by direct methods and refined by full-matrix least-squares on F^2, with the program SHELX97[38] in the WINGX[39] package. All non-hydrogen atoms except those involved in disorders were refined with anisotropic displacement parameters. The disordered parts are the PF$_6$ anions in [**3**]PF$_6$ and [**4**]PF$_6$, a cod ligand in [**4**]PF$_6$ and another cod ligand in [**9**](PF$_6$)$_2$·CH$_2$Cl$_2$, and were refined with isotropic displacement parameters and with restraints in the geometry. Hydrogen atoms were included in calculated positions except those ones of carbon atoms bonded to the metals, which were located in difference-Fourier maps. All of them were refined riding on the corresponding atom with an isotropic displacement parameter related to that of the bonded atom. The highest electronic residuals were observed in close proximity of the metal centers and make no chemical sense.

CCDC-696922 (**2**), 696923 (**3**), 696924 ([**3**]PF$_6$), 696925 ([**4**]PF$_6$), 696926 ([**7**]BF$_4$), and 696927 ([**9**](PF$_6$)$_2$·CH$_2$Cl$_2$) contain the supplementary crystallographic data for this paper. These data can be obtained free of charge from the Cambridge Crystallographic Data Center via www.ccdc.cam.ac.uk/data_request/cif.

Acknowledgements

The generous financial support from MEC-FEDER (Project CTQ2005-06807), Gobierno de Aragón (GA, Project PM36/2007), the University of Amsterdam, and the Netherlands Organization for Scientific Research (NWO-CW) is gratefully acknowledged. V.P. thanks CSIC for an I3P postdoctoral contract.

---

[1] D. Astruc, *Electron Transfer and Radical Processes in Transition-Metal Chemistry*, **1995**, Wiley-VCH, New York.
[2] See for example: B. de Bruin, D. G. H. Hetterscheid, A. J. J. Koekkock, H. Grützmacher, *Prog. Inorg. Chem.* **2007**, *55*, 247–354.
[3] a) P. Maire, M. Königsmann, A. Sreekanth, J. Harmer, A. Schweiger, H. Grützmacher, *J. Am. Chem. Soc.* **2006**, *128*, 6578–6580; b) T. Büttner, J. Geier, G. Frison, J. Harmer, C. Calle, A. Schweiger, H. Schönberg, H. Grützmacher, *Science* **2005**, *307*, 235–238.
[4] a) M. Königsmann, N. Donati, D. Stein, H. Schönberg, J. Harmer, A. Sreekanth, H. Grützmacher, *Angew. Chem.* **2007**, *119*, 3637–3640; *Angew. Chem. Int. Ed.* **2007**, *46*, 3567–3570; b) N. Donati, M. Königsmann, D. Stein, L. Udino, H. Grützmacher, *C. R. Chim.* **2007**, *10*, 721–730.
[5] a) H. Arita, K. Ishiwata, S. Kuwata, T. Ikariya, *Organometallics* **2008**, *27*, 493–496; b) K. Ishiwata, S. Kuwata, T. Ikariya, *Organometallics* **2006**, *25*, 5847–5849; c) S. Thewissen, M. D. M. Reijnders, J. M. M. Smits, B. de Bruin, *Organometallics* **2005**, *24*, 5964–5972; d) C. Tejel, M. A. Ciriano, M. Bordonaba, J. A. López, F. J. Lahoz, L. A. Oro, *Chem. Eur. J.* **2002**, *8*, 3128–3138; e) C. Tejel. M. A. Ciriano, M. Bordonaba, J. A. López, F. J. Lahoz, L. A. Oro, *Inorg. Chem.* **2002**, *41*, 2348–2355; f) H. Matsuzaka, T. Kamura, K. Ariga, Y. Watanabe, T. Okubo, T. Ishii, M. Yamashita, M. Kondo, S. Kitagawa, *Organometallics* **2000**, *19*, 216–218; g) R. Dorta, A. Togni, *Helv. Chim. Acta* **2000**, *83*, 119–127; h) J.-J. Brunet, J.-C. Daran, D. Neibecker, L. Rosenberg, *J. Organomet. Chem.* **1997**, *538*, 251–256; i) M. K. Kolel-Veetil, M. Rahim, A. J. Edwards, A. L Rheingold, K. J. Ahmed, *Inorg. Chem.* **1992**, *31*, 3877–3878; j) A. L. Casalnuovo, J. C. Calabrese, D. Milstein, *Inorg. Chem.* **1987**, *26*, 971–973.
[6] L. A. Oro, M. A. Ciriano, C. Tejel, M. Bordonaba, C. Graiff, A. Tiripicchio, *Chem. Eur. J.* **2004**, *10*, 708–715.
[7] P. Zhao, C. Krug, J. F. Hartwig, *J. Am. Chem. Soc.* **2005**, *127*, 12066–12073.
[8] a) E. Sola, F. Torres, M. V. Jiménez, J. A. López, S. E. Ruiz, F. J. Lahoz, A. Elduque, L. A. Oro, *J. Am. Chem. Soc.* **2001**, *123*, 11925–11932; b) M. V. Jiménez, E. Sola, F. J. Lahoz, L. A. Oro, *Organometallics* **2005**, *24*, 2722–2729.
[9] M. K. Kolel-Veetil, A. L. Rheingold, K. J. Ahmed, *Organometallics* **1993**, *12*, 3439–3446.
[10] C. Tejel, M. A. Ciriano, J. A. López, S. Jiménez, M. Bordonaba, L. A. Oro, *Chem. Eur. J.* **2007**, *13*, 2044–2053.
[11] *Aziridines and Epoxides in Organic Synthesis*, (Ed.: A. K. Yudin), Wiley-VCH; Weinheim, Germany, **2006**.
[12] a) K. Arai, S. Li, M. M. Dalter, K. Ohta, Y. Yamashita, S. Kobayashi, *J. Am. Chem. Soc.* **2007**, *129*, 8103–8111; b) Z.-B. Luo, J.-Y. Wu, X.-L. Hou, L.-X. Dai, *Org. Biomol. Chem.* **2007**, *5*, 3428–3430; c) J. D. G. Watson, L. Yu, A. K. Yudin, *Acc. Chem. Res.* **2006**, *39*, 194–206.
[13] a) J. E. Ney, J. P. Wolfe, *J. Am. Chem. Soc.* **2006**, *128*, 15414–15422; b) B. L. Lin, C. R. Clough, G. L. Hillhouse, *J. Am. Chem. Soc.* **2002**, *124*, 2890–2891.
[14] R. Bobka, J. N. Roedel, B. Neumann, T. Nigst, I.-P. Lorenz, *Polyhedron* **2008**, *27*, 955–961, and references therein.
[15] C. Tejel, J. M. Villoro, M. A. Ciriano, J. A. López, E. Eguizábal, F. J. Lahoz, V. I. Bakhmutov, L. A. Oro, *Organometallics* **1996**, *15*, 2967–2978.
[16] N. G. Connely, D. J. H. Emslie, P. Klangsinsirikul, P. H. Rieger, *J. Phys. Chem. A* **2002**, *106*, 12214–12220.
[17] D. G. H. Hetterscheid, J. Kaizer, E. Reijerse, T. P. J. Peters, S. Thewissen, A. N. J. Blok, J. M. M. Smits, R. de Gelder, B. de Bruin, *J. Am. Chem. Soc.* **2005**, *127*, 1895–1905.
[18] D. G. H. Hetterscheid, M. Klop, R. J. N. A. M Kicken, J. M. M. Smits, E. J. Reijerse, B. de Bruin, *Chem. Eur. J.* **2007**, *13*, 3386–3405.
[19] Considering the large amount of parameters contributing to the shape and HFI multiplets in the spectrum of [**4**]$^+$, it is not clear how unique the obtained fit is to the particular set of parameters in Table 4.
[20] J. C. Jeffery, F. G. A. Stone, I. Topaloğlu, *Polyhedron* **1993**, *12*, 319–325.
[21] B. E. Hodson, D. Ellis, T. D. McGrath, J. J. Monaghan, G. M. Rosair, A. J. Welch, *Angew. Chem.* **2001**, *113*, 737–739; *Angew. Chem. Int. Ed.* **2001**, *40*, 715–717; .
[22] A. D. Burrows, M. Green, J. C. Jeffery, J. M. Lynam, M. F. Mahon, *Angew. Chem.* **1999**, *111*, 3228–3230; *Angew. Chem. Int. Ed.* **1999**, *38*, 3043–3045; .
[23] a) M. Martín, E. Sola, O. Torres, P. Plou, L. A. Oro, *Organometallics* **2003**, *22*, 5406–5417; b) R. Dorta, A. Togni, *Organometallics* **1998**, *17*, 5441–5444.
[24] D. G. H. Hetterscheid, B. de Bruin, J. M. M. Smits, A. W. Gal, *Organometallics* **2003**, *22*, 3022–3024.
[25] D. R. Russell, P. A. Tucker, *J. Organomet. Chem.* **1977**, *125*, 303–312.
[26] G. W. Bushnell, D. O. K. Fjeldsted, S. R. Stobart, M. J. Zaworotko, *J. Chem. Soc. Chem. Commun.* **1983**, 580–581.
[27] T. L. Cairns, *J. Am. Chem. Soc.* **1941**, *63*, 871–872.
[28] R. Usón, L. A. Oro, J. Cabeza, *Inorg. Synth.* **1985**, *23*, 126–130.
[29] H. B. Gray, D. N. Hendrickson, Y. S. Sohn, *Inorg. Chem.* **1971**, *10*, 1559–1563.
[30] a) R. Ahlrichs, M. Bär, H.-P. Baron, R. Bauernschmitt, S. Böcker, M. Ehrig, K. Eichkorn, S. Elliott, F. Furche, F. Haase, M. Häser, C. Hättig, H. Horn, C. Huber, U. Huniar, M. Kattannek, A. Köhn, C. Kölmel, M. Kollwitz, K. May, C. Ochsenfeld, H. Öhm, A. Schäfer,

U. Schneider, O. Treutler, K. Tsereteli, B. Unterreiner, M. von Arnim, F. Weigend, P. Weis, H. Weiss, Turbomole Version 5, January **2002**. Theoretical Chemistry Group, University of Karlsruhe; b) O. Treutler, R. Ahlrichs, *J. Chem. Phys.* **1995**, *102*, 346–354; c) Turbomole basis-set library, Turbomole Version 5, see (a); d) A. Schäfer, H. Horn, R. Ahlrichs, *J. Chem. Phys.* **1992**, *97*, 2571–2577; e) D. Andrae, U. Haeussermann, M. Dolg, H. Stoll, H. Preuss, *Theor. Chim. Acta* **1990**, *77*, 123–141; f) A. Schäfer, C. Huber, R. Ahlrichs, *J. Chem. Phys.* **1994**, *100*, 5829–5835.

[31] a) PQS version 2.4, **2001**, Parallel Quantum Solutions, Fayetteville, Arkansas, USA (the Baker optimizer is available separately from PQS upon request); b) J. Baker *J. Comput. Chem.* **1986**, *7*, 385–395.

[32] a) C. Lee, W. Yang, R. G. Parr, *J. Chem. Phys. J. Chem. Phys.* **1988**, *37*, 785; b) A. D. Becke *J. Chem. Phys.* **1993**, *98*, 1372–1377; c) A. D. Becke *J. Chem. Phys.* **1993**, *98*, 5648–5652; d) All calculations were performed by using the Turbomole functional “b3-lyp”, which is not identical to the Gaussian “B3LYP” functional.

[33] Some references and reviews on DFT approaches to EPR parameters: a) E. van Lenthe, A. van der Avoird, P. E. S. Wormer, *J. Chem. Phys.* **1997**, *107*, 2488–2498; b) E. van Lenthe, A. van der Avoird, P. E. S. Wormer, *J. Chem. Phys.* **1998**, *108*, 4783–4796; c) F. Neese, *Curr. Opin. Chem. Biol.* **2003**, *7*, 125–135; d) F. Neese, E. Solomon in *Magnetoscience—From Molecules to Materials*, (Eds.: J. S. Miller, M. Drillon), Wiley, New York, **2003**, pp. 345–466; e) G. Peng, J. Nichols, E. A. McCullough, J. Spence, *Inorg. Chem.* **1994**, *33*, 2857–2864.

[34] a) E. J. Baerends, D. E. Ellis, P. Ros, *Chem. Phys.* **1973**, *2*, 41–51; b) L. Versluis, T. Ziegler, *J. Chem. Phys.*, **1988**, *88*, 322–328; c) G. te Velde, E. J. Baerends, *J. Comput. Phys.* **1992**, *99*, 84–98; d) C. Fonseca Guerra, J. G. Snijders, G. te Velde, E. J. Baerends, *Theor. Chem. Acc.* **1998**, *99*, 391–403.

[35] a) A. D. Becke, *Phys. Rev. A* **1988**, *38*, 3098–3100; b) J. P. Perdew, *Phys. Rev. B* **1986**, *33*, 8822–8824.

[36] G. Schaftenaar, J. H. Noordik, *J. Cold Reg. Eng. J. Comput. Aided Mol. Des.* **2000**, *14*, 123–134.

[37] G. M. Sheldrick, *SADABS*, Bruker AXS, Madison, WI, **1997**.

[38] G. M. Sheldrick, *SHELXL-97*, *Program for Crystal Structure Refinement*, University of Göttingen, Göttingen, Germany, **1997**.

[39] L. J. Farrugia, *J. Appl. Crystallogr.* **1999**, *32*, 837.

Received: August 5, 2008